Wavelet decomposed dual-time scale crystal plasticity FE model for analyzing cyclic deformation induced crack nucleation in polycrystals

2009 Modelling Simul. Mater. Sci. Eng. 17 064009

(http://iopscience.iop.org/0965-0393/17/6/064009)

Modelling Simul. Mater. Sci. Eng. **17** (2009) 064009 (30pp) doi:10.1088/0965-0393/17/6/064009

Wavelet decomposed dual-time scale crystal plasticity FE model for analyzing cyclic deformation induced crack nucleation in polycrystals

M Anahid, P Chakraborty, D S Joseph and S Ghosh

Computational Mechanics Research Laboratory, Department of Mechanical Engineering, The Ohio State University, Columbus, OH 43210, USA

E-mail: ghosh.5@osu.edu

Received 31 March 2009, in final form 1 August 2009
Published 24 August 2009
Online at stacks.iop.org/MSMSE/17/064009

Abstract

A microstructure sensitive criterion for dwell fatigue crack initiation in polycrystalline alloys is proposed in this paper. Local stress peaks due to load shedding from time dependent plastic deformation fields in neighboring grains are responsible for crack initiation in dwell fatigue. A calibrated and experimentally validated crystal plasticity finite element model (CFEM) is employed for predicting slip system level stresses and strains. Vital microstructural features related to the grain morphology and crystallographic orientations are accounted for in the FEM by construction of microstructures that are statistically equivalent to those observed in OIM scans. The output of the FEM is used to evaluate the crack initiation condition in the post processing stage. The functional form of the criterion is motivated from the similarities in the stress fields and crack evolution criteria ahead of a crack tip and dislocation pile-up. A specific model is developed for estimating the pile-up length necessary for the nucleation criterion using the notion of geometrically necessary dislocations. The crack nucleation criterion is calibrated and validated by using experimental data obtained from ultrasonic crack monitoring techniques. In order to be able to model a large number of cycles to failure initiation, a dual-time scaling algorithm is proposed using wavelet induced decomposition. The algorithm decouples the governing equations into two sets of problems corresponding to two different time scales. One is a long time scale (low frequency) problem characterizing a cycle-averaged solution, while the other is a short time scale (high frequency) problem for a remaining oscillatory portion. The method significantly reduces the computational time till crack initiation.

1. Introduction

Reduction in the life of titanium alloys under dwell fatigue loading is attributed to their susceptibility to room temperature creep [1]. During the hold period in each dwell cycle, certain favorably oriented microstructural regions undergo significant plastic straining due to slip on favorably oriented slip systems. This results in a rise in the local stress in adjacent unfavorably oriented grains in an attempt to maintain compatibility, a phenomenon known as load shedding [2]. This local stress rise has been found to cause early crack initiation under dwell fatigue loading relative to normal fatigue loading conditions, for which there is no hold period [3].

Accurate prediction of dwell fatigue crack nucleation in polycrystalline alloys has received significant research attention in recent times. Conventional fatigue analysis methods by, e.g., the stress-life or strain-life approaches, or damage tolerant approaches show significant scatter in their predictions due to lack of underlying physics based mechanisms and information about the actual material microstructure. A material microstructure based detailed mechanistic model for fatigue crack nucleation is seen as a promising alternative to such empiricism with a higher probability of accurate fatigue failure prediction. Such a model should have the following characteristics.

(i) Accurate description of material behavior through a crystal plasticity based model: the microstructural response of the aerospace alloy Ti-6242 is modeled using a size and rate dependent anisotropic elastic-crystal plasticity constitutive model that has been developed and experimentally validated in [2, 4–6]. Microstructural features such as grain size, grain neighborhood distributions and grain orientations are accounted for in a statistically equivalent sense in the model in [7–9].
(ii) Physics-based crack nucleation criterion that accounts for the effects of inhomogeneities in the microstructure: the proposed crack nucleation model developed in this work is motivated by similarities in the functional forms of the stress fields and crack evolution criteria ahead of a crack tip and dislocation pile-up, respectively [10]. The criterion incorporates an effective mixed mode stress acting on a slip plane, defined as a combination of normal and shear stresses to account for mode mixity. The criterion also accounts for the non-local effects of the dislocation pile-up in the adjacent grains, which is incorporated through a non-local plastic strain and its gradient. The dislocation pile-up length is estimated from an effective dislocation density, which is a cumulative effect of slip on multiple slip systems. The crack initiation due to the effects of dislocation pile-up is a highly non-local problem to which a coarse-graining approximation is made here. The details of the computational procedure for evaluating this criterion are discussed in section 2.2.1. The crack initiation model is calibrated and validated with a few experimental results.
(iii) Efficient algorithm to accurately simulate the evolution of microstructural variables till crack initiation: accommodation of the large number of cycles to failure, as observed in the experiments, is computationally very expensive to simulate using conventional FEM with a single time scale. In these conventional methods of numerical time integration with semi-discretization, each cycle is resolved into a large number of time steps over which integration is performed. A high resolution in the time steps is required for each cycle in the entire loading process. Typical studies in cyclic deformation with 3D crystal plasticity in the literature [11–13] simulate a small number of cycles ($\sim$100) and the results are subsequently extrapolated to thousands of cycles for making fatigue predictions. This can lead to considerable error in the evolution of variables at the microstructural level and consequently in fatigue life predictions. It is desirable to conduct simulations for a significantly high number of cycles to reach local

states of damage initiation and growth. This presents significant challenges due to the variation in time scales ranging from the scale of each cycle to that of the entire process, requiring high resolution to predict damage evolution and crack propagation. The method of direct separation of motions (MDSM) has been traditionally used to study the vibratory response under the application of high frequency loads [14, 15]. The method involves defining two separate integro-differential equations, one each for the high and low frequency components of the response. The high frequency component is either approximated or is calculated explicitly and is used in the integro-differential equation for the low frequency response. However, this method is based on the assumption that all variables are either locally periodic or almost periodic in the temporal domain. The application of this method, e.g. in [16, 17], cannot be extended to crystal plasticity solutions showing considerable localization and non-periodic response with evolving plastic variables. In [18], cyclic averaging together with asymptotic expansion of the variables in the time domain has been proposed as a basis of the multi-time scale relation. However, the asymptotic expansion methods do not work in the case of fully reversed loading or $R = -1$, for crystal plasticity models. Large oscillations present in plastic variables during reversible loading conditions lead to dominant higher order terms that do not conform to the requirements of decaying contributions with additional terms in the asymptotic series for crystal plasticity simulations. To avert this problem, a wavelet induced decomposition of the cyclic behavior is proposed as a basis of multi-time scaling in crystal plasticity simulations in this work.

The organization of the paper is as follows. The finite element (FE) model for dwell fatigue crack initiation is presented in section 2, where a method for estimating the dislocation pile-up length required in the proposed crack nucleation criterion is developed from geometrically necessary dislocations (GNDs). A wavelet based multi-time scaling scheme is introduced in section 3. A brief introduction to wavelets is given in section 3.1, while the decomposition into coarse and fine scale behavior is developed in section 3.2. In section 3.3, the associated modified FE framework is presented. The application of the multi-time scale approach to a simplified one-dimensional problem and to study the cyclic behavior of Ti-6242 is shown in section 3.4, with some concluding remarks in section 4.

2. Crystal plasticity FE model (CPFEM) for dwell fatigue crack initiation

2.1. Crystal plasticity based constitutive model

The α/β forged Ti-6242 is a biphasic polycrystalline alloy, which consists of colonies of transformed β phase in a matrix of the primary α phase. The primary α phase consists of equiaxed grains with an hcp structure whereas the transformed β colonies have alternating α(hcp) and β(bcc) laths. The alloy considered in this study consists of 70% primary α and 30% transformed β grains. To incorporate the effect of various microstructural parameters, a size and time dependent large strain crystal plasticity based FE model has been developed in [2, 4–6, 19]. A homogenized model of the $\alpha + \beta$ phase colony regions in the Ti-6242 microstructure has been developed in [4]. The plastic part of the crystal plasticity equations involves a combined effect of slip on multiple slip systems. The plastic slip rate $\dot{\gamma}^\alpha$ on the αth slip system has a power law dependence on the resolved shear stress (τ^α) and the slip system deformation resistance (g^α) which is given as

$$\dot{\gamma}^\alpha = \dot{\tilde{\gamma}} \left| \frac{\tau^\alpha - \chi^\alpha}{g^\alpha} \right|^{1/m} \text{sign}\,(\tau^\alpha - \chi^\alpha)\,. \tag{1}$$

Here m is the material rate sensitivity parameter, $\dot{\tilde{\gamma}}$ is the reference plastic shearing rate and χ^{α} is the back stress that accounts for kinematic hardening in cyclic deformation [2]. The evolution of the slip system deformation resistance is assumed to be controlled by both statistically stored dislocations (SSDs) corresponding to homogenous plastic deformation and GNDs that accommodate the incompatibility of the plastic strain field. This is expressed as

$$\dot{g}^{\alpha} = \sum_{\beta} q^{\alpha\beta} h^{\beta} |\dot{\gamma}^{\beta}| + \frac{k_0 \alpha^2 G^2 b}{2\left(g^{\alpha} - g_{\mathrm{o}}^{\alpha}\right)} \sum_{\beta} \lambda^{\beta} |\dot{\gamma}^{\beta}|, \tag{2}$$

where h^{β} in the first term of equation (2) is the self-hardening rate and $q^{\alpha\beta}$ is a matrix describing the latent hardening. The second term accounts for the effect of GNDs on the work hardening [20], in which k_0 is a dimensionless material constant, G is the elastic shear modulus, b is the Burgers vector, g_{o}^{α} is the initial deformation resistance and α is a non-dimensional constant taken to be $\frac{1}{3}$ in this work [21]. λ^{β} is a slip plane lattice incompatibility measure which can be expressed for each slip system as a function of slip plane normal ($\boldsymbol{n}^{\beta}$) and another incompatibility tensor ($\boldsymbol{\Lambda}$) as

$$\lambda^{\beta} = \left(\boldsymbol{\Lambda}\boldsymbol{n}^{\beta} : \boldsymbol{\Lambda}\boldsymbol{n}^{\beta}\right)^{1/2}. \tag{3}$$

The dislocation density tensor $\boldsymbol{\Lambda}$, introduced by Nye [22], gives a direct measure of GND density. Nye's tensor can be expressed using the curl of the plastic part of the deformation gradient tensor $\boldsymbol{F}^{\mathrm{p}}$, which is available from the CPFEM output data, as

$$\Lambda = \nabla^{T} \times \boldsymbol{F}^{\mathrm{p}}. \tag{4}$$

Numerically, the derivatives of plastic deformation gradient $\partial \boldsymbol{F}^{\mathrm{p}}/\partial \boldsymbol{x}$, which are necessary to calculate $\nabla^{T} \times \boldsymbol{F}^{\mathrm{p}}$, are obtained at each integration point within the elements using shape function based interpolation of nodal values of $\boldsymbol{F}_{\alpha}^{\mathrm{p}}$ as

$$\frac{\partial \boldsymbol{F}^{\mathrm{p}}}{\partial \boldsymbol{x}} = \frac{\partial}{\partial \boldsymbol{x}} \left(\sum_{\alpha} N_{\alpha} \boldsymbol{F}_{\alpha}^{\mathrm{p}} \right) = \sum_{\alpha} \frac{\partial N_{\alpha}}{\partial \boldsymbol{x}} \boldsymbol{F}_{\alpha}^{\mathrm{p}}. \tag{5}$$

The nodal values of $\boldsymbol{F}_{\alpha}^{\mathrm{p}}$ are calculated from the integration points in the surrounding elements using a weighted averaging scheme.

$$\boldsymbol{F}_{\alpha}^{\mathrm{p}} = \frac{\sum_{\beta} W_{\beta} \left(\boldsymbol{F}_{\mathrm{IP}}^{\mathrm{p}}\right)_{\beta}}{\sum_{\beta} W_{\beta}}. \tag{6}$$

Here $\left(\boldsymbol{F}_{\mathrm{IP}}^{\mathrm{p}}\right)_{\beta}$ corresponds to the plastic deformation gradient at the βth integration point surrounding the αth nodal point inside the grain. The weighting function is expressed in [23] as $W_{\beta} = \left(1/(2\pi)^{3/2} l^3\right) \exp\left(-r_{\beta}^2/2l^2\right)$, in which r_{β} is the distance between the node at which the plastic deformation gradient is being evaluated and an element integration point. This weighting function decays to zero beyond a critical distance corresponding to l. Numerical sensitivity analysis on the effect of l on $\boldsymbol{F}^{\mathrm{p}}$ at different nodes concludes that $\boldsymbol{F}_{\alpha}^{\mathrm{p}}$ does not vary much for $l \geqslant 5\,\mu$m. Hence l is assumed to be $5\,\mu$m in this study. To account for grain size effects on the initial deformation resistance g_{o}^{α}, a Hall–Petch type relation with various characteristic length scales that depend on the slip direction has been incorporated in the model [6, 19]. Material properties for each of the constituent phases and individual slip systems in the crystal plasticity model and the parameters in the size effect relationship are calibrated and provided in [4–6]. Other parameters used in equation (2) are listed in table 1. Details of the microstructural morphology are accounted for in the model, through accurate phase volume fractions, and orientation distributions that are statistically equivalent to those observed in OIM scans as detailed in [7–9]. The computational model is validated by comparing the results of simulations of constant strain rate and creep tests in [4–6, 19].

Table 1. Parameters used in the hardening evolution equation (equation (2)).

Material parameter	Value
Shear modulus G	48 GPa
Magnitude of Burgers vector b	0.30 nm
Material constant k_0	2

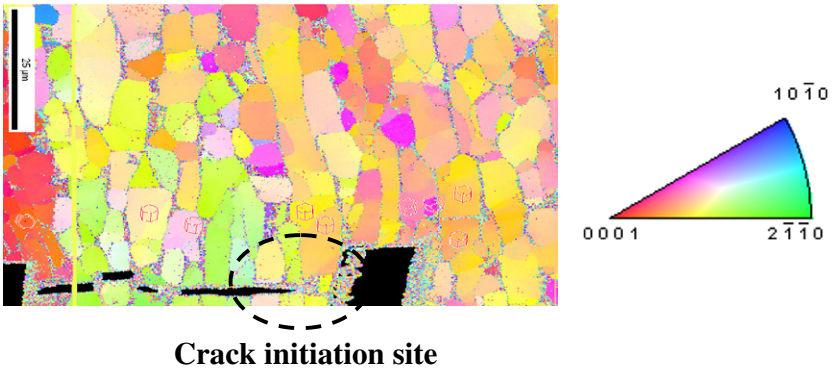

Figure 1. OIM scan of the critical primary crack initiation site in the MS1 microstructure.

2.2. Crack nucleation criterion accounting for dislocation pile-up

Extensive experimental studies on the relation between crack evolution and crystallographic orientations in Ti-6242 have been conducted in [24] using quantitative tilt fractography and electron back scattered diffraction (EBSD) techniques in SEM. Figure 1 shows an OIM micrograph of a crack initiation site for a Ti-6242 sample in dwell fatigue, which is found to consist of facets that form on the basal plane of the primary α grains (hcp) lying almost perpendicular to the principal tensile loading direction. It has been observed that the angle between the loading axis and the '$\boldsymbol{c}$' axis, i.e. the '$\boldsymbol{c}$' axis orientation (θ_c) of the grains at the failure site is quite small ($\sim$0–30°). Furthermore, the failure site shows a low prism activity with Schmid factor (SF) $\sim$0–0.1 and a moderate basal activity with a SF $\sim$0.3–0.45. However, the region surrounding the failure site has a high prismatic and basal activity with a SF $= \sim$0.5. Thus, it may be inferred that while crack initiation occurs in a region that is unfavorably oriented for slip it is surrounded by grains that are favorably oriented for slip. In other words, crack initiates in a hard oriented grain surrounded by soft oriented grains. The observations suggest time dependent accumulation of stress in hard oriented grains due to load shedding with increasing plastic deformation in the surrounding soft grains, which is responsible for crack initiation in Ti-6242 under creep and dwell loading.

Crack nucleation phenomena have been considered at different length scales in the literature [25]. In this section, a crack nucleation criterion that was originally proposed in [26, 27] at the length scale of individual grains is improved for better accuracy and consistency. High stresses that develop near the tip of dislocation pile-ups at grain boundary barriers are often responsible for micro-crack nucleation. Various dislocation level fatigue failure models, e.g. [10, 28–31], have discussed the equivalence in the dependences of crack evolution ahead of dislocation pile-ups and at crack tips. This equivalence in the functional forms has been utilized in [26] to develop a grain-level crack nucleation criterion. The framework for micro-crack nucleation in [26] builds upon the fracture criterion proposed in [32], where catastrophic fracture occurs when the strain energy release rate is sufficient to overcome the rate of surface

energy needed for breaking of bonds, as well as energy dissipation due to plastic flow. A crack nucleation criterion is postulated with the understanding that a brittle crack is nucleated in the hard α-grain due to stress concentration caused by dislocation pile-up in the neighboring soft grains. In this criterion, micro-cracking is triggered when an effective stress on a slip system reaches a critical value. Following the discussions in [32], the effective stress for mixed mode crack nucleation is expressed in terms of the slip system normal and tangential stress components as

$$T_{\text{eff}} = \sqrt{\langle T_{\text{n}} \rangle^2 + \beta T_{\text{t}}^2}, \tag{7}$$

where the stress component normal to a given slip plane is given as $T_{\text{n}} = n_i^b \left(\sigma_{ij}\, n_j^b \right)$, in terms of the Cauchy stress tensor σ_{ij} and the components of unit outward normal to the slip plane n_i^b. Only the tensile normal stress $\langle T_{\text{n}} \rangle$, represented by the McCauley bracket $\langle\ \rangle$, contributes to the effective stress since compressive stresses do not contribute to crack opening. The shear stress component T_{t} is obtained by the vector subtraction of T_{n} from the stress vector on the plane, i.e. $T_{\text{t}} \boldsymbol{t}^b = \boldsymbol{T} - T_{\text{n}} \boldsymbol{n}^b$, where $\boldsymbol{t}^b$ is the unit vector tangent to the plane. β is a shear stress factor, which is used to assign different weights to the normal and shear traction components for mixed mode. It is defined as the ratio of the shear to normal fracture toughness of the material, i.e. $\beta \approx (K_{\text{IIC}}/K_{\text{IC}})$ in [33].

Continuous dislocation pile-ups at a barrier, e.g. at the boundary of a soft grain adjacent to a hard grain, have been shown to be equivalent to cracks, e.g. in [10], in the way they cause stress concentration and crack nucleation at their tip. The dislocation pile-up length in the crack nucleation model is hence assumed to scale with the pre-crack length in the corresponding crack tip initiation models [32]. Analogously, the hard grain crack nucleation criterion, ahead of dislocation pile-ups in adjacent soft grains has an inverse square root dependence on the pile-up length d, and is stated as

$$T_{\text{eff}} = \sqrt{\langle T_{\text{n}} \rangle^2 + \beta T_{\text{t}}^2} \geqslant \frac{R_{\text{c}}}{\sqrt{d}} \tag{8a}$$

or equivalently,

$$R = T_{\text{eff}} \cdot \sqrt{d} \geqslant R_{\text{c}}, \tag{8b}$$

where R_{c} is a parameter that depends on the material elastic properties, as well as on the critical strain energy release rate G_c. It has the units of stress intensity factor (MPa$\sqrt{\mu\text{m}}$). A value of $\beta = 0.7071$ suggested for Ti-64 alloys in [34] is used in this study. Sensitivity analysis with different values of β indicate that T_{eff} is not very sensitive to β for $\langle \boldsymbol{c}+\boldsymbol{a} \rangle$ oriented hard grains, since $T_{\text{n}} \gg T_{\text{t}}$. As more dislocations are added to the pile-up with time, the pile-up length d in the soft grain increases. This implies a smaller T_{eff} to initiate a crack with increasing plastic deformation and pile-up.

The methodology developed in [26, 27] to obtain the dislocation pile-up length from the crystal plasticity FE solution, assumed that the total dislocation density per unit area ρ^A follows the same distribution function as the density function per unit length ρ^l for single slip. To overcome the limitations of this assumption, a direct method to obtain a more accurate estimation of dislocation pile-up length is proposed in this work.

2.2.1. Direct numerical method for estimating the dislocation pile-up length d. For estimating the dislocation pile-up length d, it is necessary to have the distribution of dislocation densities inside the grain. However, the CPFEM in [4–6] does not explicitly have dislocation density as a state variable. Hence the plastic strains and its gradients available from the results of the

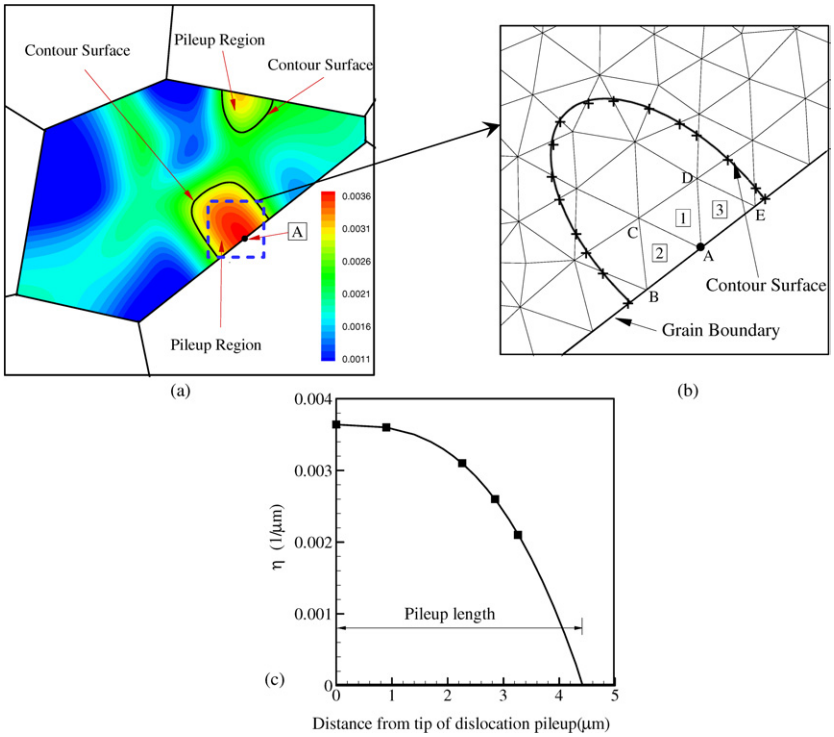

Figure 2. Estimating the dislocation pile-up length d: (a) distribution of η inside a representative soft grain, (b) FE mesh around a dislocation pile-up tip, (c) variation of η with distance from tip of dislocation pile-up.

crystal plasticity FE simulations are used to estimate the dislocation pile-up length d. This contributes to the non-locality aspect of the crack nucleation criterion.

In the dislocation glide model, the plastic deformation characterized by $\boldsymbol{F}^{\mathrm{p}}$ results in an incompatible, non-physical intermediate configuration. The lattice incompatibility can be measured by the closure failure of a line integral along a Burgers circuit $\bar{\Gamma}$, which can be quantified with the net Burgers vector $\boldsymbol{b}$ of all dislocations threading the region $\bar{\Omega}$ bounded by the circuit. This is considered as a measure for GNDs density that is related to a surface integral of the curl of $\boldsymbol{F}^{\mathrm{p}}$ over a referential surface Ω by application of the classical Stokes' theorem

$$\boldsymbol{b} = \oint_{\bar{\Gamma}} \mathrm{d}\bar{\boldsymbol{x}} = \oint_{\bar{\Gamma}} \boldsymbol{F}^{\mathrm{p}} \mathrm{d}\boldsymbol{X} = \int_{\Omega} \boldsymbol{\Lambda}.\boldsymbol{n}\mathrm{d}\Omega, \tag{9}$$

where $\boldsymbol{n}$ is the unit normal to the surface Ω and $\boldsymbol{\Lambda}$ is the Nye's dislocation tensor given in equation (2). In this work, the norm of Nye's dislocation tensor η is used as the measure for density of GNDs. Components of $\boldsymbol{\Lambda}$ are evaluated at each quadrature point using the algorithm described in section 2.1. Figure 2(a) shows the distribution of η inside a representative soft grain. The maximum values of η occur at the grain boundary and the values decrease with increasing distances from the grain boundary. The pile-up length d for each soft grain region is evaluated using the following procedure. It should be noted that all calculations are done in actual 3D space, but for simplicity reasons the procedure is explained in 2D representation.

(i) The nodal values of η are calculated from the integration points in the surrounding elements using the weighted averaging scheme described in section 2.1.

(ii) Among all boundary nodes, those with a higher value of η than their adjacent nodes are considered as the tip of a dislocation pile-up (like node A in figures 2(a) and (b)).

(iii) For each dislocation pile-up tip in the soft grain, the centroid of contour surfaces is determined for a few values of $\eta \leqslant \eta_{\text{tip}}$ using a geometric discretization scheme of the contour surface, where η_{tip} is the value of η at the tip of dislocation pile-up. Figure 2(b) shows the FE mesh around a dislocation pile-up tip (node A) as well as a contour surface corresponding to a value $\eta_c \leqslant \eta_{\text{tip}}$. The goal is to find the intersection points of this surface and finite elements edges to be able to determine the centroid of the contour surface. In the following, the geometric discretization scheme of the contour surface is briefly explained as shown in figure 2(b):

(a) All nodes are assigned an index which initially equals zero (except for node A which is equal to 1). If the index equals 1 it means that the node has already been read.
(b) The elements inside the soft grain which are associated with node A are specified (elements number 1, 2 and 3).
(c) The value of η is read for all nodes of the specified elements in (b) which have zero index value (nodes B, C, D and E). If $\eta > \eta_c$ for a particular node, the index of that node changes to 1. If $\eta > \eta_c$, one of the intersection points of the contour surface and elements edges is obtained by doing an interpolation along the element edge to find a point in which $\eta = \eta_c$.
(d) Steps (b) and (c) are repeated for all nodes whose index has changed to 1 in step (c). The geometric discretization scheme of the contour surface is complete when no nodal index changes to 1 in step (c).
(e) After obtaining all intersection points, the contour surface can be approximated by a combination of triangles and quadrilaterals (which are the intersection of the contour surface and 3D elements).

(iv) The distance from the centroid to the tip of dislocation pile-up is measured for different values of $\eta \leqslant \eta_{\text{tip}}$ and plotted in figure 2(c).

(v) The pile-up length d, which is assumed to be the distance between the centroid of the $\eta = 0$ contour surface and the tip of dislocation pile-up, is calculated by extrapolating the graph to the zero value of η. This is shown in figure 2(c).

The effective traction T_{eff} at a point in the hard grain as well as the dislocation pile-up length d evaluated for adjacent softer grain from the proposed procedure can be used in equations (8a) and (8b) to calculate the effective nucleation variable R. R is checked for every grain pair in the CPFEM in the post-processing stage. The condition posed in equations (8a) and (8b) is non-local, in that the stress required to initiate a crack at a point in the hard grain depends on the gradient of plastic strain in the neighboring soft grain as well.

2.3. Calibration and validation of the nucleation criterion

Three dwell fatigue experimental tests are considered to calibrate and validate the crack nucleation model as described in [24]. Three sample α/β forged Ti-6242 microstructures labeled MS1, MS2 and MS3 that differ in orientation, misorientation and micro-texture distribution, as discussed in [26], are considered in this work. Mesh convergence studies have been done in [26] and subsequent simulations are performed using the converged mesh. Each trapezoidal wave in the dwell cycles of these tests has a maximum applied load of 869 MPa (95% of yield stress), a hold time of 2 min, a loading/unloading time of 1 s and a stress ratio (ratio of minimum to maximum load) equal to zero [35, 36]. In the experimental

observations, samples MS1, MS2 and MS3 fail after 352, 663 and 447 cycles, respectively. Crack growth in samples MS2 and MS3 is monitored through micro-radiographic images taken by interrupting the experiment every 15 cycles. The plot of the evolution of crack length with the number of cycles is extrapolated backwards to zero crack length to determine the approximate number of cycles to crack initiation for primary and secondary cracks in these samples. The extrapolated number of cycles to crack initiation is found to be 530 for MS2 and 380 for MS3. This information on the incremental evolution of crack length with number of cycles is, however, not available for sample MS1, though the complete life is available. Hence the number of cycles to initiation cannot be determined for this sample. The results in [35] suggest that primary crack initiation in dwell fatigue generally occurs in the range 80–90% of total number of cycles to failure. Assuming that crack initiation in MS1 also occurs in this range, the number of cycles to nucleation corresponds to 282–317 cycles for this sample. This is used for calibration of the range of material parameter R_c in this study. This calibrated range of values of R_c is then used to predict the lower and upper bound of values of crack initiation cycles in samples MS2 and MS3, which are subsequently compared with the experimental values.

The methodology described in [26] is used for the construction of 3D microstructures from 2D OIM scans. The microstructures are created from observations of two specific sites in the material samples, namely (i) a critical region, in the vicinity of a dwell fatigue failure, and (ii) a non-critical region, away from it. The first sample considered is MS1. Two orientation imaging microscopy or OIM scans are performed on this sample; the first on a small critical region surrounding the primary crack tip as shown in figure 1, while the second on a non-critical region away from the crack. Two FE models of statistically equivalent simulated microstructures at the critical and non-critical regions are developed for analysis. In the development of the crack initiation model, it is expected that the initiation criterion will be met at some location in the critical FE model, but will not be satisfied in the non-critical FE model.

2.3.1. Calibration of R_c for α/β forged Ti-6242. The material parameter R_c in the RHS of equations (8*a*) and (8*b*) is calibrated from the results of 2 min dwell fatigue FE simulations of the microstructure MS1 at the critical region for 352 cycles. The representative cube of dimensions 65 μm × 65 μm × 65 μm for the MS1 microstructure consists of 949 grains which is discretized into a FE mesh of 78 540 tetrahedron elements as shown in figure 3. Based on the observations in [35], initiation is assumed at two alternative percentages of the total life, namely 80% and 90%, which correspond to 282 and 317 cycles. To calibrate R_c corresponding to the two percentages, the variable R in equation 8(b) is determined for all grain pairs at the end of 282 and 317 cycles. The hard grain of the grain pair with maximum value of R is located and the evolution of this maximum R with the number of cycles is plotted in figure 4(*a*). Assuming initiation to have occurred at these fractions, the value of R may be equated to R_c from equation 8(b). For the two cases, the threshold values are determined to be $R_{c(80\%)} = 3260.09\,\text{MPa}\sqrt{\mu\text{m}}$ and $R_{c(90\%)} = 3354.92\,\text{MPa}\sqrt{\mu\text{m}}$. These parameters are subsequently used for predicting crack initiation in other experiments and studies.

The FE simulation of the microstructure MS1 at the non-critical region is also conducted for 2 min dwell loading conditions and the value of R is evaluated for all grain pairs. Figure 4(*b*) plots the evolution of the maximum R as a function of the cycles. The maximum R reached at the end of 352 cycles is only $2279\,\text{MPa}\sqrt{\mu\text{m}}$, which is less than both the threshold values of R_c. Consequently, the criterion does not predict a crack initiation in this non-critical region as expected from the experimental observation.

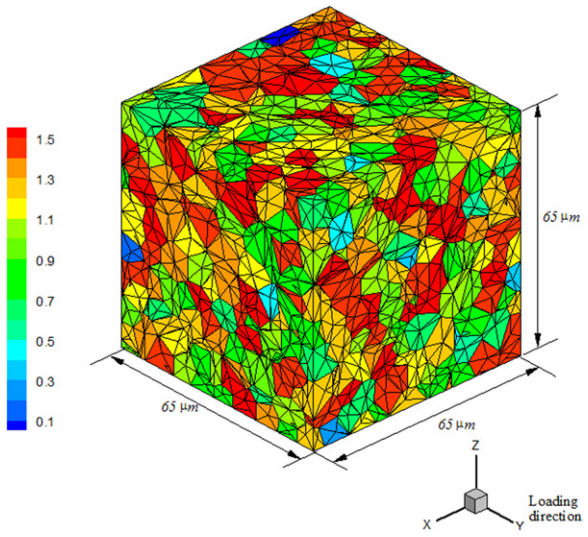

Figure 3. FE model for polycrystalline Ti-6242, which is statistically equivalent to the OIM scan of the critical region of microstructure MS1. Also shown is the contour of '*c*' axis orientation distribution (radians).

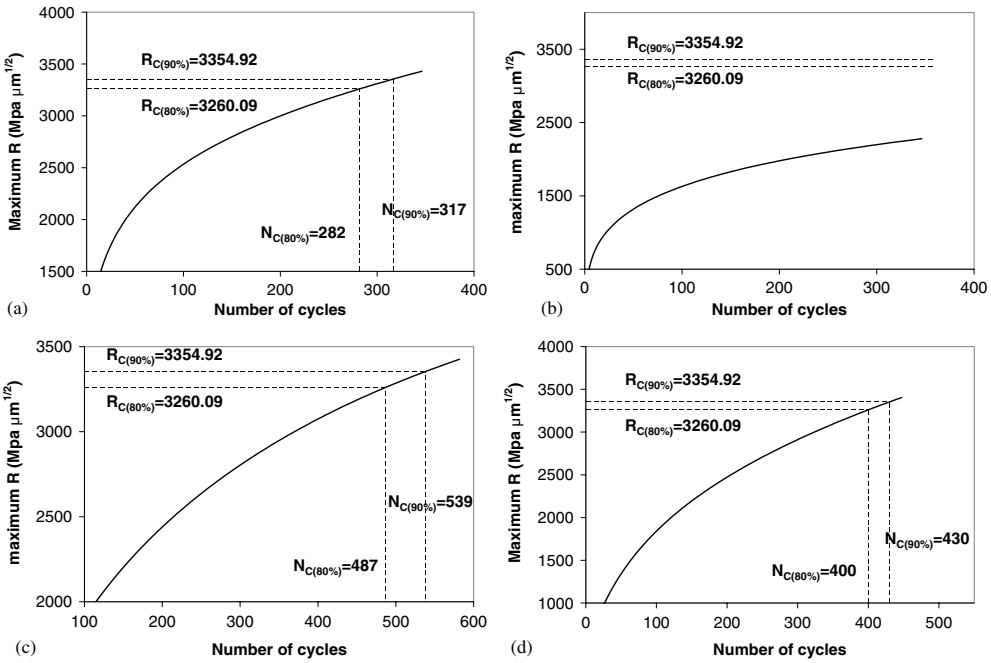

Figure 4. Evolution of the maximum R over number of cycles for the FE models of microstructures: (*a*) MS1 critical region, (*b*) MS1 non-critical region, (*c*) MS2 and (*d*) MS3.

2.3.2. Predictions and analysis with samples MS2 and MS3. For the MS2 microstructure, the FE model is generated to be statistically equivalent to an OIM scan surrounding one of the secondary cracks in the failed sample. The crack initiation for that crack is determined to occur at 530 cycles from experimental observations in [35] as described in [26]. The 2 min

Table 2. Comparison of predicted cycles to crack initiation with experimentally observed life.

Microstructure label	Time to crack initiation (experiment)	Time to crack initiation (predicted)		% Relative error	
		Calibrated at 80% life	Calibrated at 90% life	Calibrated at 80% life	Calibrated at 90% life
MS2	530 cycles	487 cycles	539 cycles	−8.18	+1.64
MS3	380 cycles	400 cycles	430 cycles	+5.26	+13.32

Table 3. Microstructural features of predicted location of crack initiation in dwell fatigue of Ti-6242.

Microstructure label	θ_c (°)	SF prism	SF basal
MS1	21.8	0.07	0.34
MS2	28.7	0.10	0.42
MS3	33.3	0.13	0.46

dwell fatigue FE simulation is performed for 663 cycles with loading conditions described in [35]. Figure 4(*c*) shows the evolution of the maximum R with cycles. The number of cycles to initiation $N_{c(80\%)}$ and $N_{c(90\%)}$ are predicted for MS2 from where the evolution curve meets the calibrated threshold values $R_{c(80\%)}$ and $R_{c(90\%)}$. The corresponding cycles to initiation are found to be $N_{c(80\%)} = 487$ and $N_{c(90\%)} = 539$. The difference with the experimentally determined value of 530 cycles is −8.18% for 80% of life and only +1.64% for 90% of life. This agreement is considered to be excellent.

Likewise, for the MS3 microstructure, the FE model is generated using statistics of the corresponding critical regions at the failure site and the 2 min dwell fatigue simulation is performed for 447 cycles. The evolution of the maximum R is plotted in figure 4(*d*). The number of cycles to initiation for MS3 are predicted to be $N_c(80\%) = 400$ and $N_{c(90\%)} = 430$. From experimental results in [35], this crack initiates at 380 cycles as described in [26]. The differences between the predicted and experimentally determined values are 5.26% for 80% of life and 13.32% for 90% of life. The results are summarized in table 2.

The experimentally determined value of the number of cycles to fatigue crack initiation in MS2 lies between the lower and upper bounds of the predicted values through simulations. However the predicted number of cycles to crack initiation in MS3 is higher than the experimentally determined value. Therefore it is important to consider the error of both predictions together. For this purpose an error analysis with an alternative reference is considered. This time instead of MS1, the parameter R_c in the crack nucleation model is calibrated with the results of dwell fatigue FE simulations of MS2 in the same way as discussed in section 2.3.1. Knowing that crack initiates after 530 cycles in MS2, the new calibrated R_c value is found to be 3339.83 MPa $\sqrt{\mu m}$. The crack nucleation model with the new calibrated R_c parameter is then used to predict the number of cycles to crack initiation in MS3. This is obtained as $N_c = 425$, which corresponds to a 12% difference with the experimentally determined value (380).

As an additional validation study, the predicted locations of crack initiation in these microstructures are examined and summarized in table 3. It can be seen that in each case, crack initiation is predicted for a grain with low prism SF (∼0–0.1) and low to moderate basal SF (∼0.3–0.45), which is consistent with the observations [24]. Also all predicted 'c' axis orientation values in the crack regions are within the high range of the experimentally observed

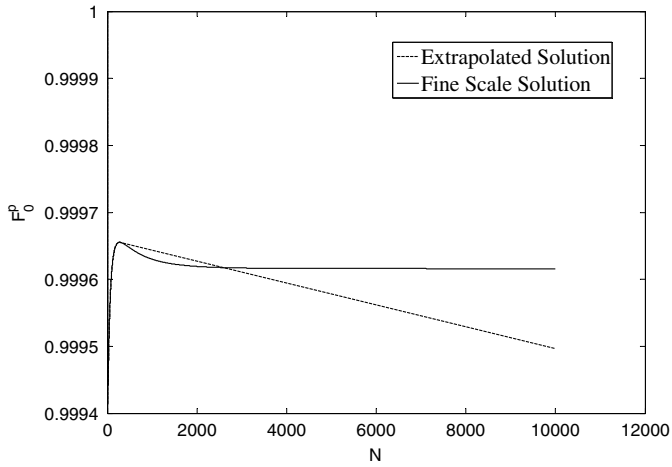

Figure 5. Extrapolated and exact solution of $F_{\mathrm{p}}(N, 0)$ of a material point.

range ($\sim$0°–30°). This implies that crack nucleation occurs in a hard grain. These results prove convincingly the predictive capability of the proposed criterion. The model is expected to be extrapolated to other materials as long as the same mechanisms for dwell fatigue hold.

In these simulations, each cycle is approximately resolved into 37 time steps for numerical integration in MARC. The number of time steps per cycle are expected to be even more for fully reversible ($R = -1$) or near fully reversible cyclic loading, in which large plastic oscillations dominate and is discussed in section 3. This will result in a large computational overhead making simulations nearly impossible if a large number of cycles are considered for failure. A clue to resolving this excessive problem is the fact that two time scales prevail for this problem, the first fine scale corresponding to the time scale of the loading cycles, and the second corresponding to the time scale of the overall material response. An efficient numerical time integration scheme that can admit decomposition of the overall response into these two naturally arising time scales is a prudent way to overcome this shortcoming. This is the subject of the next section.

3. Wavelet decomposed dual-time scale model for CPFEM simulations

In the introduction, limitations of the extrapolation based methods and dual-time scaling approach with asymptotic expansion of variables in the time domain are discussed. The limitation of extrapolation based methods is illustrated by considering an eight element polycrystalline model subjected to cyclic loading. Figure 5 shows the difference between the exact and extrapolated solutions for the plastic deformation gradient at a material point at the beginning of each cycle. Extrapolation is performed based on the gradient (in time) at the 300th cycle. The results clearly show significant error in the predicted values based on extrapolation. The asymptotic expansion methods [16–18] are not suitable when large oscillations are encompassed in the plastic variables. These large oscillations arise particularly in the case of fully reversed loading ($R \to -1$). These oscillations are not numerical in nature nor do they depend on the hardening law. They are connected to the oscillations in the resolved shear stress in the flow rule (equation (1)). This effect is shown in the context of a 1D viscoplastic model subjected to two cases of cyclic displacement loading: (i) $R \sim -0.32$,

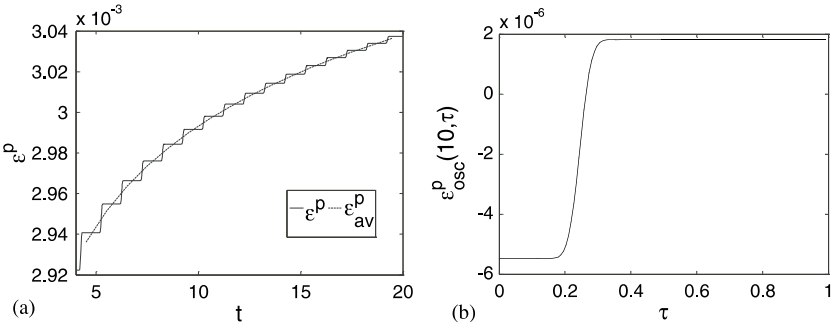

Figure 6. For $R \sim -0.32$ (a) evolution of ε^{p} for 20 cycles, (b) evolution of $\varepsilon^{\mathrm{p}}_{\mathrm{osc}}$ over the 10th cycle.

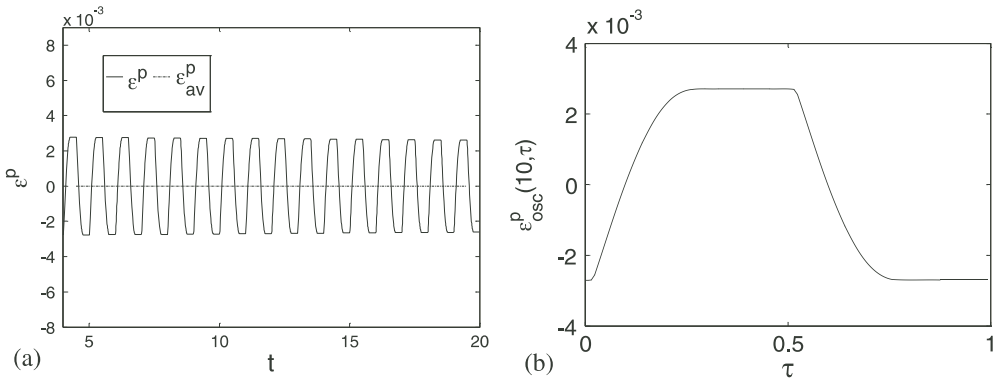

Figure 7. For $R = -1.001$ (a) evolution of ε^{p} for 20 cycles, (b) evolution of $\varepsilon^{\mathrm{p}}_{\mathrm{osc}}$ over the 10th cycle.

(ii) $R = -1.001$. As can be observed from figures 6 and 7, the $R = -1.001$ case show significantly higher oscillations in the plastic strain compared with the $R \sim -0.32$ case for the same value of peak strain. Further, although the loading is reversible (in case (ii)), the plastic strain is not reversible due to the evolution in the hardening parameter as shown by figure 8.

To avert these problems, a novel wavelet induced decomposition of the cyclic behavior is proposed as a basis of multi-time scaling in crystal plasticity simulations. Unlike some of the previous approaches [16, 17], the proposed method makes no assumption on the local periodicity of the solution or asymptotic behavior of the variables. The method is valid under all loading conditions including fully reversible or $R \to -1$, and does not require a calibration step unlike [18]. It can therefore be extended easily for any general set of time evolution equations.

The method is motivated from the response of a state variable (y) at a material point undergoing cyclic deformation obeying a viscoplastic constitutive relationship such as crystal plasticity, as shown in figure 9. Clearly, there exist two time scales in the material response: a fast varying fine time scale (τ) response showing rapid changes within a cycle and a slow varying coarse time scale response. The value of the plastic strain at the beginning of a certain

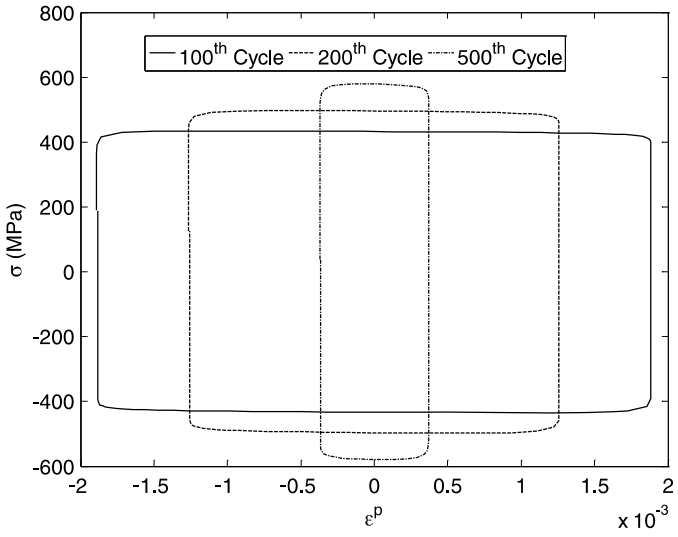

Figure 8. Plot of σ versus ε^{p} for $R = -1.001$.

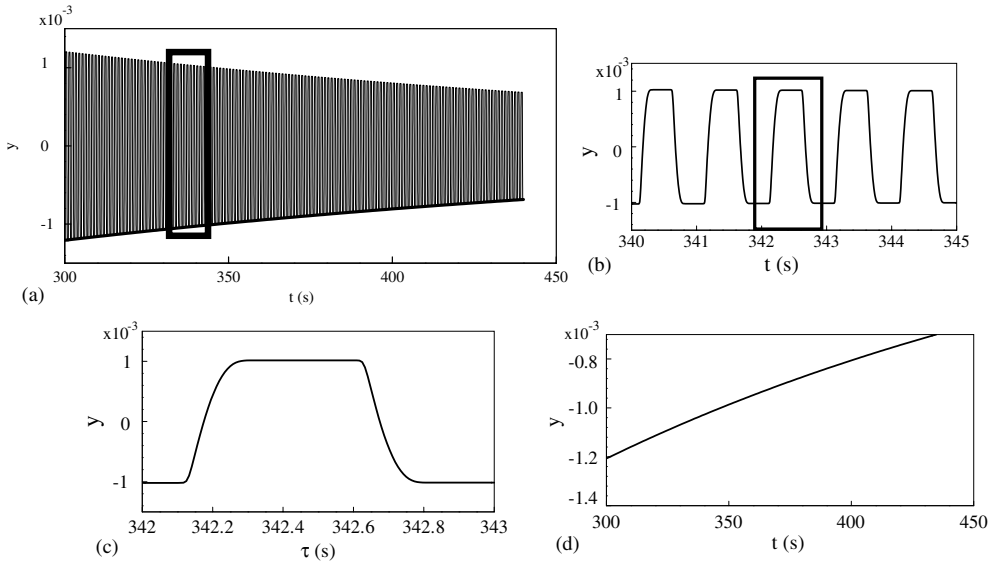

Figure 9. Decoupling the fine and coarse time scale responses for a state variable: (*a*) fine scale solution, (*b*), (*c*) zoomed in fine-scale solution, (*d*) decoupled coarse scale solution.

cycle (y^{o}) is considered as a coarse time scale variable. This does not vary in the fine time scale (τ) within the cycle but varies across cycles. Hence, it can be considered to be purely a function of the cycle number N, i.e. $y^{\mathrm{o}} = y^{\mathrm{o}}(N)$. However the variation of the coarse scale variable y^{o} is coupled with its corresponding fine scale evolution ($y(N, \tau)$). In order to completely decouple the coarse and fine scale effects, the primary variable, in this case the displacement field (u) over a particular cycle, is resolved over an appropriate basis $\psi_k(\tau)$ which is purely a function of the fine scale τ. In addition, the coefficients of the strain $\varepsilon^k(N)$ can be derived

from the coefficients of displacements:

$$u(x,t) = u(x,N,\tau) = \sum_k c^k(x,N)\psi_k(\tau),$$
$$\varepsilon(x,t) = \varepsilon(x,N,\tau) = \sum_k \frac{\mathrm{d}c^k}{\mathrm{d}x}(x,N)\psi_k(\tau) = \sum_k \varepsilon^k(x,N)\psi_k(\tau). \tag{10}$$

The coefficients of the displacement field $c^k(x,N)$ are solved using a FE framework in the scale of cycles. The fine scale behavior, representing the variation within each cycle, is generated through the representation as a linear combination of the wavelet basis functions. The wavelet basis functions remain the same for every cycle in the entire loading history. Therefore, the coarse scale behavior is associated with the cycle number N and the fine scale behavior with τ which varies between 0 and the time period T.

The objective then is to obtain a coarse time scale equation of the form

$$\frac{\mathrm{d}y^{\mathrm{o}}}{\mathrm{d}N} = f\left(y^{\mathrm{o}}(N), \varepsilon^k(N)\right). \tag{11}$$

A single integration step of equation (11) can be used to jump over many cycles (ΔN), resulting in significant computational savings and is discussed in section 3.2.

The method developed here requires a suitable basis for decomposing the displacement (and hence the strain/deformation gradient) fields over time as in equation (10). The basis function chosen should satisfy the following conditions:

(i) The basis functions should be orthogonal.
(ii) The number of coefficients which evolve as the loading progresses should be as small as possible.
(iii) The basis functions required for refining the signal up to a certain resolution should be known *a priori*.

The basis of Fourier-series functions appears to be a natural fit for representing the response of cyclic problems. However they suffer from the following shortcomings:

(i) The signals considered here are defined over a finite support defined by the time period of loading. Since Fourier basis functions have infinite support, using a finite set of Fourier coefficients can lead to instabilities such as the Gibbs phenomenon with spurious oscillations at regions where the signal is cut off . This in turn can lead to inaccuracies in the evaluation of the coarse scale equation.
(ii) While using a finite set of Fourier coefficients, the dominant coefficients (from the infinite set) needed to match the signal to a given resolution are not known without trial and error.

The wavelet basis avoids these shortcomings and hence is the basis of choice for the multi-time scale approach developed here.

3.1. A brief overview of wavelet basis functions

A wavelet basis spans the space of square integrable functions $L^2(R)$ through translation and dilation of the scaling function ϕ [37, 38]:

$$f(\tau) = \sum_m \sum_n C_{mn}\phi_{mn}(\tau), \tag{12}$$

where $\phi_{mn} = 2^{m/2}\phi(2^m\tau - n)$, m corresponds to the dilatation and n corresponds to the translation of the function ϕ. The scaling function and the mother wavelet function for the

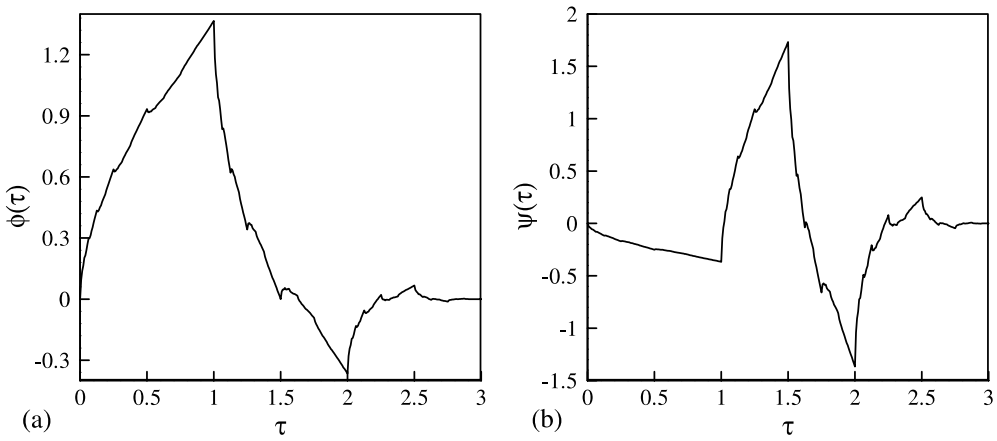

Figure 10. Scaling function for Daubuchies4 wavelet: (*a*) scaling function, (*b*) mother wavelet.

Daubechies4 wavelet, used in this work, is shown in figure 10. If V_m denotes the subspace at a given resolution m, generated by the function ϕ_{mn} through translation, then the sequence

$$\{0\} \subset \ldots \subset V_{-1} \subset V_0 \subset V_1 \subset \ldots \subset V_m \subset V_{m+1} \subset \ldots \subset L^2(R) \tag{13}$$

forms a multiresolution analysis of the space $L^2(R)$. Corresponding to the above sequence a space W_m with the basis $2^{m/2}\psi(2^m\tau - n)$ can also be defined. This gives the orthogonal difference between the spaces V_m and V_{m+1} i.e. $V_{m+1} = V_m \oplus W_m$. The function ψ is called the mother wavelet and it spans the spaces W_m through translation and dilatation. If a signal is available at resolution m i.e. it belongs to the space V_m, it can be split into two orthogonal components belonging to V_{m-1}(at a lower resolution) and W_{m-1} (which gives the difference signal between the two successive resolutions).

$$\begin{aligned} f^m(\tau) &= \sum_n \langle f, \phi_{m-1,n}\rangle \phi_{m-1,n} + \sum_n \langle f, \psi_{m-1,n}\rangle \psi_{m-1,n} \\ &= \sum_n a^{m-1,n}\phi_{m-1,n} + \sum_n d^{m-1,n}\psi_{m-1,n} \\ &= f^{m-1} + \sum_n d^{m-1,n}\psi_{m-1,n}, \end{aligned} \tag{14}$$

where $a^{m-1,n}$ and $d^{m-1,n}$ are called the approximation and the detail coefficients. The function f^{m-1} is an approximation of the function f^m at a lower resolution. The same procedure can be carried out on f^{m-1} and subsequent approximations, each time reducing the resolution by half and generating an additional set of detail coefficients. Therefore, the final decomposition consists of two approximation coefficients (in the case of Daubuchies4 wavelets) and the remaining detail coefficients.

The procedure in equation (14) can be thought of as the action of a high pass and low pass filter as discussed [38]. The approximation coefficients correspond to the low pass filter and the detail coefficients to the high pass filter, given as

$$\begin{Bmatrix} \boldsymbol{a}^{m-1} \\ \boldsymbol{d}^{m-1} \end{Bmatrix} = \begin{bmatrix} \boldsymbol{H} \\ \boldsymbol{G} \end{bmatrix} a^m, \tag{15}$$

where $\boldsymbol{a}^m$ are the 2^m approximation coefficients at resolution m which are split into 2^{m-1} approximation ($\boldsymbol{a}^{m-1}$) and 2^{m-1} detail coefficients ($\boldsymbol{d}^{m-1}$) at level $m-1$. The matrices $\boldsymbol{H}$ and

$\boldsymbol{G}$ each of size $2^{m-1} \times 2^m$ (for Daubechies 4 with periodic extension) are given as

$$\begin{bmatrix} \boldsymbol{H} \\ \boldsymbol{G} \end{bmatrix} = \begin{bmatrix} h_1 & h_2 & h_3 & h_4 & & & & & \\ & & h_1 & h_2 & h_3 & h_4 & \dots & & \\ & & \vdots & \vdots & \vdots & \vdots & \vdots & & \\ h_3 & h_4 & & & & & & h_1 & h_2 \\ g_1 & g_2 & g_3 & g_4 & & & & & \\ & & g_1 & g_2 & g_3 & g_4 & \dots & & \\ & & \vdots & \vdots & \vdots & \vdots & \vdots & & \\ g_3 & g_4 & & & & & & g_1 & g_2 \end{bmatrix}, \tag{16}$$

where h_i and g_i are the filter coefficients which satisfy the relation

$$\begin{aligned} \phi(t) &= \sqrt{2} \sum_{k=1}^{N_s} h_k \phi(2t-k), \\ \psi(t) &= \sqrt{2} \sum_{k=1}^{N_s} g_k \phi(2t-k). \end{aligned} \tag{17}$$

The Daubechies4 wavelets have four filter coefficients ($N_s = 4$) which are given by

$$\begin{aligned} h_1 &= \frac{1+\sqrt{3}}{4\sqrt{2}}, \quad h_2 = \frac{3+\sqrt{3}}{4\sqrt{2}}, \quad h_3 = \frac{3-\sqrt{3}}{4\sqrt{2}}, \quad h_4 = \frac{1-\sqrt{3}}{4\sqrt{2}} \\ g_1 &= \frac{1-\sqrt{3}}{4\sqrt{2}}, \quad h_2 = \frac{-3+\sqrt{3}}{4\sqrt{2}}, \quad h_3 = \frac{3+\sqrt{3}}{4\sqrt{2}}, \quad h_4 = \frac{-1-\sqrt{3}}{4\sqrt{2}}. \end{aligned} \tag{18}$$

The process in equation (15) can be repeated till $m = 2$ for Daubuchies4 and the resulting approximation and detail coefficients stored in a single array $\boldsymbol{c}$. Since all the operations are linear, the entire multiresolution decomposition can be represented as

$$c^k = \sum_{l=0}^{N_f} T_{kl} f(\tau_l) \qquad k = 1 \dots N_f, \tag{19}$$

where τ_l are the $N_f = 2^m$ fine scale points at which the function is sampled, c^k are the wavelet approximation and detail coefficients and $\boldsymbol{T}$ is an orthogonal matrix containing the filter coefficients constructed by the repeated application of equation (16) to the lowest approximation level.

3.1.1. Properties of wavelets. The wavelets form a suitable basis for representing the fine scale behavior due to the following properties:

(i) *Compact support:* Each wavelet basis spans a finite domain. As a result the wavelet decomposition does not exhibit spurious instabilities like the Gibbs phenomena unlike the Fourier series functions.

(ii) *Multiresolution:* For a given resolution of the fine scale behavior, the space of basis functions is well defined and finite, unlike in the Fourier basis. This implies that representing the fine scale behavior at a given resolution will require an *a priori* known set of basis as opposed to Fourier basis functions, where the required basis need to be found by trial and error.

(iii) *Number of coefficients:* The number of coefficients required can be minimized if an approximate nature of the response is known before. For example, in the case of dwell or triangular loading, the response over a cycle might have regions which are almost linear which makes Daubechies4 wavelets an ideal choice, since they are able to represent linear behavior exactly leading to fewer coefficients. These are used in this work.

3.2. Coarse scale constitutive relationship

In this section, the coarse scale evolution equations of the form in equation (11) are developed. The evolution of a state variable y in general can be considered as

$$\dot{y} = f\left(y, \varepsilon(\tau)\right) = f\left(y, \varepsilon^k(N), \tau\right), \tag{20}$$

where ε^k are the (known) wavelet coefficients of the applied strain. Given the initial value of y for a cycle N and the strain components, the value of y at any fine scale time point (τ) in the cycle can be obtained as

$$y\left(N,\tau\right) = y\left(N,0\right) + \int_0^\tau f\left(y, \varepsilon^k\left(N\right), \tau'\right) \mathrm{d}\tau' = y_\mathrm{o}\left(N\right) + \int_0^\tau f\left(y, \varepsilon^k\left(N\right), \tau'\right) \mathrm{d}\tau', \tag{21}$$

where $y_0\left(N\right) \overset{\Delta}{=} y\left(N,0\right)$. If T is the time period, then using the continuity of y across cycles i.e. $y\left(N,T\right) = y\left(N+1,0\right) = y_\mathrm{o}\left(N+1\right)$ the coarse time scale derivative of y can be defined as

$$\frac{\mathrm{d}y_\mathrm{o}}{\mathrm{d}N} = \frac{y\left(N,T\right) - y\left(N,0\right)}{T} = \frac{1}{T}\int_0^T f\left(y, \varepsilon^k\left(N\right), \tau\right) \mathrm{d}\tau = Y_0\left(y_\mathrm{o}, \varepsilon^k\right). \tag{22}$$

The integral in the above equation is evaluated numerically using an implicit scheme. The above equation represents the coarse scale evolution or rate of change of the initial value of state variable y per cycle. In this paper a second order implicit backward difference scheme is utilized to integrate equation (22). The scheme is governed by the equation

$$\begin{aligned} &a_1 y_\mathrm{o}\left(N+\Delta N\right) - a_2 y_\mathrm{o}\left(N\right) + a_3 y_\mathrm{o}\left(N-\Delta N_\mathrm{p}\right) = \Delta N \frac{\mathrm{d}y_\mathrm{o}}{\mathrm{d}N}\left(N+\Delta N\right) \qquad \text{with} \\ &a_1 = \frac{\left\{(r+1)^2 - 1\right\}}{\left\{(r+1)^2 - (r+1)\right\}}, \qquad a_2 = \frac{(r+1)^2}{\left\{(r+1)^2 - (r+1)\right\}}, \qquad a_3 = \frac{1}{\left\{(r+1)^2 - (r+1)\right\}}. \end{aligned} \tag{23}$$

Here ΔN and ΔN_p are the cycle jumps corresponding to the current and previous steps and $r = \left(\Delta N / \Delta N_\mathrm{p}\right)$.

3.2.1. Coarse scale crystal plasticity equations. The multi-time scale approach developed in the previous section is applied to the crystal plasticity constitutive model for Ti-6242 [4, 19]. The model is summarized below:

$$\begin{aligned} &\boldsymbol{F} = \boldsymbol{F}^\mathrm{e}\boldsymbol{F}^\mathrm{p}, \\ &\dot{\boldsymbol{F}}^\mathrm{p}\boldsymbol{F}^{\mathrm{p}^{-1}} = \sum_\alpha \dot{\gamma}^\alpha \boldsymbol{s}^\alpha \otimes \boldsymbol{m}^\alpha, \\ &\boldsymbol{S}^* = \boldsymbol{C}\boldsymbol{E}^\mathrm{e} \qquad \boldsymbol{E}^\mathrm{e} = \frac{1}{2}\left(\boldsymbol{F}^{\mathrm{e}T}\boldsymbol{F}^\mathrm{e} - \boldsymbol{I}\right), \\ &\boldsymbol{\sigma} = \frac{1}{J}\boldsymbol{F}^\mathrm{e}\boldsymbol{S}^*\boldsymbol{F}^T, \\ &\dot{\gamma}^\alpha = \dot{\tilde{\gamma}}\left|\frac{\tau^\alpha - \chi^\alpha}{g^\alpha}\right|^{1/m} \mathrm{sign}(\tau^\alpha - \chi^\alpha) \qquad \text{where } \tau^\alpha = \left(\boldsymbol{F}^{\mathrm{e}T}\boldsymbol{F}^\mathrm{e}\right)\boldsymbol{S}^* : \left(\boldsymbol{s}^\alpha \otimes \boldsymbol{m}^\alpha\right), \\ &\dot{\chi}^\alpha = c\dot{\gamma}^\alpha - \mathrm{d}\chi^\alpha\left|\dot{\gamma}^\alpha\right|, \end{aligned} \tag{24}$$

where $\boldsymbol{F}$ is the deformation gradient, $\boldsymbol{F}^{\mathrm{p}}$ is the plastic deformation gradient, $\dot{\gamma}^{\alpha}$, χ^{α}, $\boldsymbol{s}^{\alpha}$ and $\boldsymbol{m}^{\alpha}$ are the slip rate, back stress, slip system direction and slip system normal, respectively, of system α, $\boldsymbol{S}^{*}$ is the second Piola–Kirchhoff stress with respect to the relaxed configuration and $\boldsymbol{\sigma}$ is the Cauchy stress at the material point. The evolution law for the hardness is given in equation (2). The evolving microstructural variables for the above model are therefore $\boldsymbol{F}^{\mathrm{p}}$, g^{α}, χ^{α} and γ^{a} (for the bcc phase). Applying the methodology in the previous section, the coarse scale evolution equations for these variables can be expressed as

$$\begin{aligned}
\frac{\mathrm{d}F_{ij}^{\mathrm{po}}}{\mathrm{d}N} &= f_{ij}\left(F_{ij}^{k}(N), F_{ij}^{\mathrm{po}}, g^{\alpha\mathrm{o}}, \chi^{\alpha\mathrm{o}}, \gamma^{a\mathrm{o}}\right),\\
\frac{\mathrm{d}g^{\alpha\mathrm{o}}}{\mathrm{d}N} &= G^{\alpha}\left(F_{ij}^{k}(N), F_{ij}^{\mathrm{po}}, g^{\alpha\mathrm{o}}, \chi^{\alpha\mathrm{o}}, \gamma^{a\mathrm{o}}\right),\\
\frac{\mathrm{d}\chi^{\alpha\mathrm{o}}}{\mathrm{d}N} &= B^{\alpha\mathrm{o}}\left(F_{ij}^{k}(N), F_{ij}^{\mathrm{po}}, g^{\alpha\mathrm{o}}, \chi^{\alpha\mathrm{o}}, \gamma^{a\mathrm{o}}\right),\\
\frac{\mathrm{d}\gamma^{a\mathrm{o}}}{\mathrm{d}N} &= \Gamma\left(F_{ij}^{k}(N), F_{ij}^{\mathrm{po}}, g^{\alpha\mathrm{o}}, \chi^{\alpha\mathrm{o}}, \gamma^{a\mathrm{o}}\right),
\end{aligned} \tag{25}$$

where F_{ij}^{po} is the initial value for the plastic deformation gradient for cycle N, $g^{\alpha\mathrm{o}}$ and $\chi^{\alpha\mathrm{o}}$ are the initial values for the hardness and back stress for slip system α corresponding to cycle N, and $\gamma^{a\mathrm{o}}$ is the initial value for the accumulated slip over all slip systems (included only for the bcc phase). F_{ij}^{k}s are the components of the deformation gradient over a wavelet basis and is given by

$$F_{ij}^{k} = \delta_{ij}\,\langle\psi_k\rangle + \sum_{k}\frac{\partial u_i^k}{\partial X_j}\psi_k \qquad \text{with } u_i^k = \int_0^T u_i\,(N,\tau)\,\psi_k\,(\tau)\,\mathrm{d}\tau. \tag{26}$$

u_i^k are the wavelet components of the displacement field $u_i\,(N,\tau)$ over the Nth cycle. The right-hand side of equation (25) is calculated based on equation (22). For example, for F_{ij}^{po},

$$\frac{\mathrm{d}F_{ij}^{\mathrm{po}}}{\mathrm{d}N} = \frac{1}{T}\int_0^T \sum_{\alpha}\dot{\gamma}^{\alpha}s_i^{\alpha}m_k^{\alpha}F_{kj}^{\mathrm{p}}\mathrm{d}\tau \tag{27}$$

with the integral evaluated numerically using the backward Euler method. Once the values of the coarse scale variables are known, the variations of the Cauchy stress ($\sigma\,(N,\tau)$) and other state variables over the cycle N can be computed.

3.3. FE framework for the coarse time scale problem

In order to utilize the coarse scale equations discussed in the previous section, a modified FE framework with the wavelet coefficients of the nodal displacements (instead of nodal displacements as in conventional FEM) as the primary solution variable is required. The nodal displacements are decomposed in terms of the wavelet basis as

$$q_i\,(N,\tau) = \sum_{k} q_i^k\,(N)\,\psi_k\,(\tau), \tag{28}$$

where q_i is the nodal displacement corresponding to the degree of freedom i in the standard FEM and q_i^k are its wavelet components. The displacement and the deformation gradient field can then be computed as

$$\begin{aligned}
u_i^k\,(X,N) &= \sum_{\alpha} N_{\alpha}q_{n(i,\alpha)}^k,\\
F_{ij}^k\,(X,N) &= \delta_{ij}\,\langle\psi_k\rangle + \sum_{\alpha}\frac{\partial N_{\alpha}}{\partial X_j}q_{n(i,\alpha)}^k,
\end{aligned} \tag{29}$$

where N_α is the shape function corresponding to node α and $n\,(i,\alpha)$ is the degree of freedom number associated with the displacement component i at node α.

A fine scale analysis is carried out initially for a few (N_0) cycles to obtain the initial displacement response and the initial values of the wavelet coefficients in equation (19).

$$q_i^k\,(N_0) = \sum_{l=0}^{N_\mathrm{f}} T_{kl} q_i\,(N_0, \tau_l) \qquad k = 1 \ldots N_\mathrm{f}, \tag{30}$$

where $q_i^k\,(N_0)$'s are the wavelet coefficients of the nodal displacements decomposed over the cycle N_0. The number of degrees of freedom for the modified problem is then $N_\mathrm{d} \times N_\mathrm{f}$, where N_d is the number of degrees freedom corresponding to the conventional FEM problem. Keeping all the wavelet coefficients might give rise to a large number of degrees of freedom and therefore to reduce their number, a scheme which selects the coefficients which are evolving the most (and hence need to be solved) as the loading progresses is required. In this work, only the wavelet coefficients which satisfy the condition $|q_i^k\,(N_0)| \geqslant \mathrm{ctol} \times \max\left(q_i^k\right)$ are considered for solution. These coefficients are denoted by $\hat{q}_i^k$ with $k = 1 \ldots N_i^{\mathrm{evol}}$, where N_i^{evol} are the number of wavelet coefficients corresponding to degree of freedom i that satisfy the aforementioned criterion. The nodal displacement variation over a given cycle then becomes

$$q_i\left(N, \tau_j\right) = \sum_{k=1}^{N_{i,\alpha}^{\mathrm{evol}}} \hat{T}_{kj}^i \hat{q}_i^k\,(N) + q_i^{\mathrm{add}}\left(\tau_j\right) \qquad j = 1 \ldots N_\mathrm{f}. \tag{31}$$

The matrix $\hat{\boldsymbol{T}}^i$ is constructed from the wavelet transform matrix $\boldsymbol{T}$ by removing the rows corresponding to the non-evolving coefficients of degree of freedom i. The constant contribution (q_i^{add}) from the non-evolving coefficients is calculated at the initial cycle N_0 and is used throughout the loading. Hence the solution variables for the modified framework are $\hat{q}_i^k$ and the number of degrees of freedom is $\sum_{k=1}^{N_\mathrm{d}} N_k^{\mathrm{evol}}$ i.e. the sum of the number of the evolving coefficients corresponding to all the displacement components at all the nodes.

The unknown wavelet coefficients for cycle N are solved using the standard weak form of the equilibrium equation, which is also decomposed into its wavelet components over the cycle.

$$f_i^k(N) = \sum_{l=0}^{N_{i\alpha}^{\mathrm{evol}}} \hat{T}_{kl}^i f_i(\tau_l) = 0 \quad \text{where } f_i(\tau_l) = \int_{V(\tau_l)} B_{ji}\sigma_j\,(N, \tau_l)\,\mathrm{d}V - \int_{S_t(\tau_l)} N_{ji}\bar{t}\,(N, \tau_l)\,\mathrm{d}S. \tag{32}$$

Here B_{ji} and N_{ji} are the matrices connecting the strain and displacement, respectively, at a point, to the nodal displacement corresponding to degree of freedom i in the conventional FEM and $\bar{t}(N, \tau)$ is the applied load over cycle N. The variation of the Cauchy stress (in Voigt form) over cycle N is obtained as a function of the nodal displacement components by solving the coarse scale equations, as described in the previous section. The Jacobian for equation (32) can be approximated as

$$\frac{\partial f_i^k}{\partial \hat{q}_j^l} = \sum_{m=1}^{N_\mathrm{f}} \hat{T}_{km}^i \frac{\partial f_i}{\partial q_j}(\tau_m) \hat{T}_{lm}^j \tag{33}$$

where $(\partial f_i/\partial q_j)(\tau)$ is the standard fine scale Jacobian for geometrically non-linear problems [39] evaluated at time point τ. This is used as an initial Jacobian for a quasi-Newton scheme [40], which is used to solve the equilibrium equations (32) .

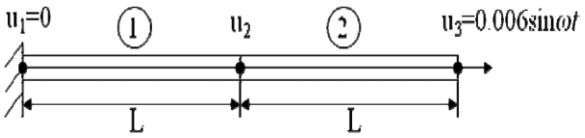

Figure 11. 1D viscoplastic model problem ($L = 1$).

3.3.1. Error criterion and step size corresponding to number of cycles. A typical step size in the coarse time scale equations corresponds to the number of cycles the numerical integration traverses. A truncation error is developed for the integration scheme to determine the optimal step size in each coarse scale increment and also to study the effect a step size has on the residual. The truncation error for the implicit second order backward difference scheme in equation (23) is expressed as

$$\delta y_0 \leqslant \left\| \frac{(r+1)^2 - (r+1)^3}{(r+1)^2 - 1} \frac{\mathrm{d}^3 y_0}{\mathrm{d}N^3} \right\| \Delta N^3 = y_{\mathrm{err}} \Delta N^3. \tag{34}$$

ΔN is the number of cycles integrated in a single step and $r = \left(\Delta N / \Delta N_{\mathrm{p}}\right)$. Equation (34) is obtained by considering the error due to second order truncation of the Taylor expansion for the variable y_0. Based on the constitutive level truncation error, the norm of the error propagated to the equilibrium residual δf is shown to be

$$\delta f = \delta f_{\mathrm{err}} \Delta N^3 \qquad \text{where } \delta f_{\mathrm{err}} = \max_{el} \left\| \int_{V^{el}} \boldsymbol{B}^{\mathrm{T}} \frac{\partial \boldsymbol{\sigma}}{\partial \boldsymbol{F}^{\mathrm{po}}} \frac{(r+1)^2 - (r+1)^3}{(r+1)^2 - 1} \frac{\mathrm{d}^3 \boldsymbol{F}^{\mathrm{po}}}{\mathrm{d}N^3} \mathrm{d}V \right\|. \tag{35}$$

For the error to be bounded by a given relative tolerance η, the maximum allowed step jump ΔN_{jump} can be estimated as

$$\Delta N_{\mathrm{jump}} \leqslant \left(\frac{\eta f_{\mathrm{err}}}{\delta f_{\mathrm{err}}} \right)^{1/3} \qquad \text{with} \quad f_{\mathrm{err}} = \sum_{el} \left\| \int_{V^{el}} \boldsymbol{B}^{\mathrm{T}} \frac{\partial \sigma}{\partial \boldsymbol{F}^{\mathrm{po}}} \boldsymbol{F}^{\mathrm{po}} \mathrm{d}V \right\|. \tag{36}$$

3.4. Numerical examples

Numerical studies are performed for a 1D viscoplastic problem described in section 3.4.1 and a 3D Ti-6242 polycrystalline problem, described in section 3.4.2. The 1D problem shows the convergence of the method with respect to coarse time steps and displacement coefficients. The 3D problem demonstrates the accuracy and efficiency of the method for Ti-6242 microstructure. A completely reversible macroscopic loading ($R \to -1$) is applied to show that the method works for stress ratios, for which the asymptotic expansion based method fails.

3.4.1. A 1D elastic–viscoplastic problem. The methodology developed is applied to study the cyclic response of a 1D model undergoing a simplified elastic–viscoplastic material response:

$$\sigma = E\left(\varepsilon - \varepsilon^{\mathrm{p}}\right), \qquad \dot{\varepsilon}^{\mathrm{p}} = \dot{a} \left| \frac{\sigma}{g} \right|^{1/m} \mathrm{sgn}(\sigma), \qquad \dot{g} = h \left| \dot{\varepsilon}^{\mathrm{p}} \right| \qquad g(0) = g_{\mathrm{o}}. \tag{37}$$

Here ε^{p} is the viscoplastic strain, g is the hardness, σ is the stress and $\dot{a}$, h, E and g_{o} are material parameters. The model consists of two, one-dimensional bar elements as shown in figure 11, with the following material properties: $E = 200\,\mathrm{GPa}$, $\dot{a} = 0.0023\,\mathrm{s}^{-1}$, $h = 100\,\mathrm{MPa}$, $g_{\mathrm{o}} = 200\,\mathrm{MPa}$ for element 1 and $g_{\mathrm{o}} = 600\,\mathrm{MPa}$ for element 2. The model is fixed at the left end and subjected to a sinusoidal loading at the right end with $\omega = 2\pi$ i.e. $T = 1\,\mathrm{s}$. In the

viscoplastic model in equation (37) the variables to be integrated using equation (23) are the initial values of the plastic strain and hardness as shown below:

$$\boldsymbol{f}^{\text{const}} = a_1\boldsymbol{\alpha}_0\left(N+\Delta N\right) - a_2\boldsymbol{\alpha}_0\left(N\right) + a_3\boldsymbol{\alpha}_0\left(N-\Delta N_{\text{p}}\right) - \Delta N\frac{\mathrm{d}\boldsymbol{\alpha}_0}{\mathrm{d}N}\left(N+\Delta N\right) = 0$$

$$\text{where} \quad \boldsymbol{\alpha}_0 = \begin{Bmatrix} \varepsilon^{p\text{o}} \\ g^{\text{o}} \end{Bmatrix}. \tag{38}$$

The derivatives are calculated using equation (22). A Newton–Raphson scheme is used to calculate $\boldsymbol{\alpha}_0(N+\Delta N)$ from equation (38).

The only unknown displacement in the model is that of node 2, which is decomposed into its wavelet coefficients. The wavelet decomposed equilibrium equation for the 1D problem over the cycle $N+\Delta N$ is

$$f^k\left(N+\Delta N\right) = \sum_{k=1}^{N_{\text{evol}}} \hat{T}_{kl}\left(\sigma_1\left(N+\Delta N,\tau_l\right) - \sigma_2\left(N+\Delta N,\tau_l\right)\right) = 0, \tag{39}$$

where σ_i corresponds to the stress in element i and N_{evol} is the number of evolving displacement coefficients. The details of the Jacobians used for the constitutive level and equilibrium iterations are given in the appendix. A criterion for the maximum size of the integration step can also be obtained similar to equation (36).

Numerical results: In this section a numerical convergence study is performed on the model subjected to a sinusoidal loading as shown in figure 11 for 2000 cycles. The loading considered here is fully reversible ($R=-1$) which is not amenable to the method discussed in [18]. The multi-time scale method is used to integrate the equations over the 'coarse' cycle scale and the results are compared with those obtained from fine scale analysis for accuracy as well as computational efficiency. The effect of the number of evolving nodal displacement wavelet coefficients chosen based on the displacement tolerance ctol and the effect of the maximum allowed step size (number of cycles) on the solution is also investigated.

Three cases are considered for the displacement tolerance criteria for selecting the number of evolving coefficients, namely ctol $= 10^{-10}$, 10^{-4}, 10^{-3}. This results in 128, 30 and 10 coefficients which are free to evolve, respectively. Corresponding to each of the three cases, four different step size bounds $\Delta N_{\max}$ on the predicted cycle increment ΔN_{jump} in equation (36) are considered. The step increment used for a coarse scale integration step is $\Delta N = \min\left(\Delta N_{\text{jump}}, \Delta N_{\max}\right)$. The value of η in equation (36) is taken to be 10^{-3}. Figure 12 shows the variation of the coarse strain variables ($\varepsilon^{p\text{o}}$ and g^{o}) as a function of cycle number N. Except for the case with very few evolving wavelet coefficients ($\sim$10) for the nodal displacement, the coarse scale results show excellent agreement with the fine scale results. When the number of coefficients is too low, refining the time step does not have any effect as seen from figure 12(*b*). This is due to the fact that there are not enough basis functions available to represent the displacement accurately regardless of the time step.

Once the coarse scale variables ($\varepsilon^{p\text{o}}$ and g^{o}) for a given cycle, along with the wavelet displacement coefficients are known, then the fine scale response for that cycle can be calculated by superimposing the wavelet bases as in equation (21). This is shown in figure 13, in which the plastic strain variation over the 2000th cycle is obtained from the coarse scale solution for different step bounds and number of evolving coefficients. Once again taking too small a number of coefficients (figure 13(*c*) with 10 coefficients) have an adverse effect on the solution. However, it is seen that the difference in response between 30 and 128 evolving nodal displacement coefficients is minimal. Therefore, a criterion needs to be developed that would give the optimal number of coefficients to evolve without sacrificing too much accuracy. Table 4 shows the effect of the number of coefficients on the computational speedup compared

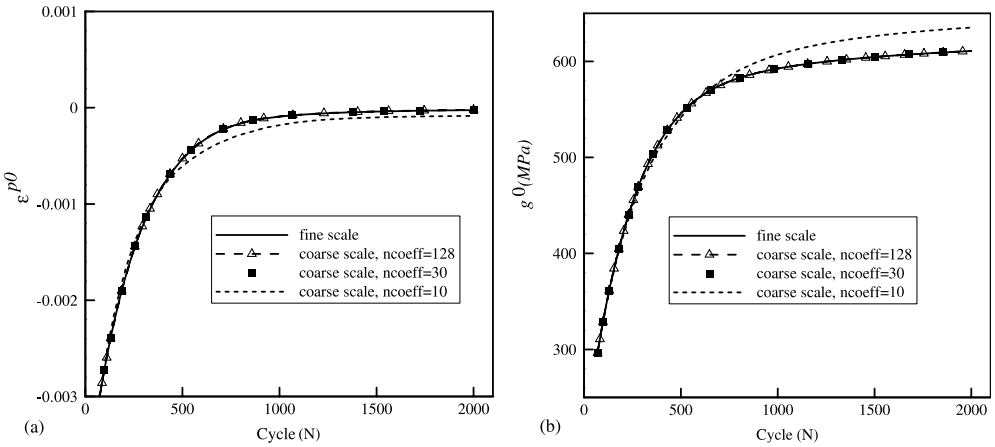

Figure 12. Variation of the coarse time variables as a function of coarse time (N): (a) initial plastic strain over cycle for element 1 with $\Delta N_{\max} = \infty$, (b) initial hardness over cycle for element 1 with $\Delta N_{\max} = 25$.

with the pure fine scale analysis and the accuracy of the result. A speedup of around 80 times is obtained without sacrificing a significant amount of accuracy for the problem considered here.

3.4.2. Multi-time scale method applied to Ti-6242 under cyclic loading. The developed model is validated for the 3D crystal plasticity equation (24) applied to Ti-6242 alloy along with size effect [5]. The model problem consists of eight element/grains with different crystallographic orientations to emulate a polycrystalline problem with hard and soft grains. To demonstrate the advantage of the current methodology for $R \to -1$ problems, a triangular pressure load with a time period of 1 s, an amplitude of 850 MPa and zero average has been considered. Fine scale simulation is carried out for the first 8 cycles and the coarse time scale approach with a starting cycle jump of 4 is used thereafter. As the problem progresses the coarse scale time step is obtained from the criterion given in equation (35). Daubechies wavelet basis has been used to decompose the nodal displacement over a cycle. All the coefficients are selected and evolved in the coarse time scale problem.

The problem is run for 10 000 cycles and compared with the fine scale simulation results. Figure 14 shows the comparison of F_0^{p} (initial value of plastic deformation gradient) between coarse and fine time scale simulations at a material point for different cycles. A similar comparison for slip system resistance g_{o}^{α} for a slip system is shown in figure 15. The shape change of displacement over different cycles for a degree of freedom and the comparison between the coarse and fine time scale solutions are shown in figure 16. The state of stress σ_{zz} of the model along the loading direction at the 10 000th cycle for both coarse and fine time scale simulation is shown in figure 17. As can be observed, the coarse time scale and fine time scale results are in excellent agreement with each other.

For the problem considered, the coarse scale method also provides a substantial time advantage. The fine scale simulation takes approximately 180 h for 10 000 cycles whereas the coarse scale simulation takes around 6 h for the same number of cycles when run on the same machine, thus giving around 30 times advantage in computational time. It is observed that the coarse scale time step (ΔN) predicted by the criterion in equation (35) increases as the problem progresses, which adds to the computational speedup.

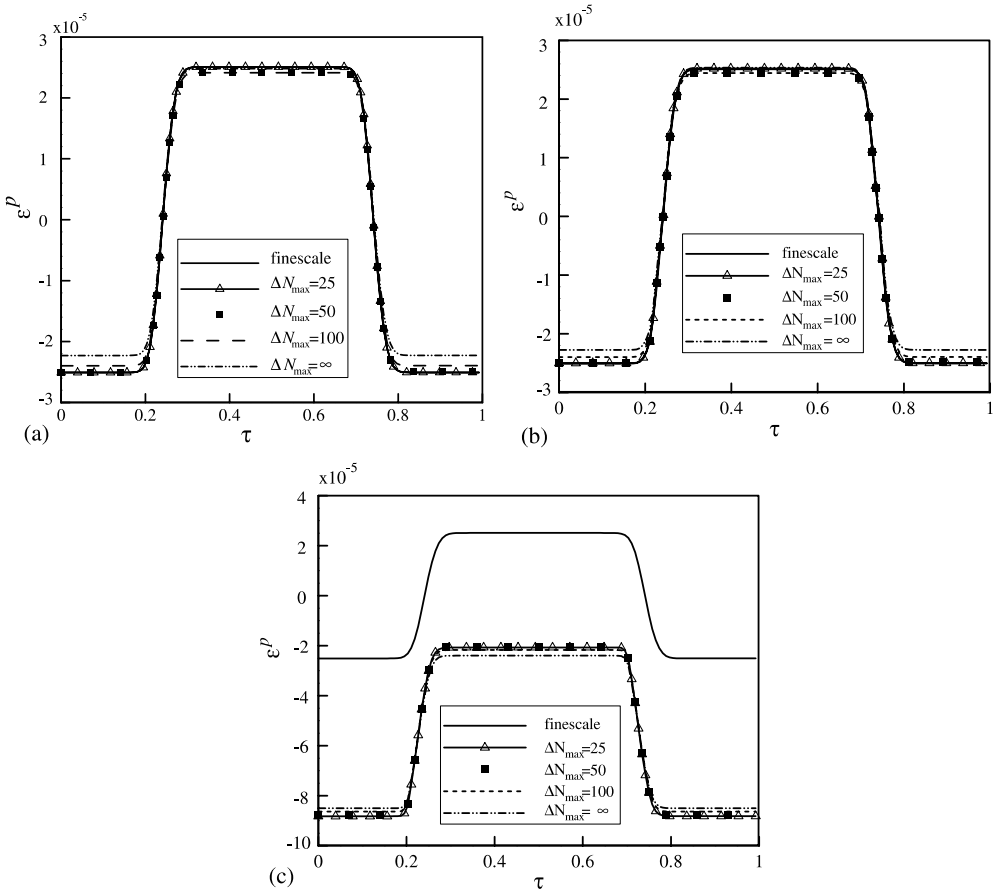

Figure 13. Reconstructed values of the plastic strain for the 2000th cycle for various step bounds $\Delta N_{\max}$ corresponding to (*a*) 128 coefficients, (*b*) 30 coefficients and (*c*) 10 coefficients.

Thus the proposed wavelet based multi-time scale technique can be used for accurate and efficient simulation of Ti-6242 alloys till crack initiation.

4. Conclusions

This paper presents the development of a microstructure sensitive crack nucleation criterion in polycrystalline alloys under cyclic deformation. An experimentally validated, rate and size dependent, crystal plasticity model is used for the computational modeling of the grain level mechanical response. The 3D FE models employed consist of statistically equivalent representations of vital microstructural characteristics of a failure site of the specimen. It is proposed that fatigue crack initiates due to stress concentration caused by the load shedding phenomenon between adjacent hard and soft grains. To predict load shedding induced crack initiation, a criterion that depends on local effective stresses in the hard grain, as well as the non-local plastic strain gradients in adjacent soft grains is proposed. The functional form of the criterion is motivated from the similarities between crack evolution at the tip of a pre-existing crack and a dislocation pile-up. It is observed that the local effective stress required to

Table 4. Effect of step size and number of coefficients on error and speedup.

Coefficient tolerance/ number of coefficients	$\Delta N_{\max}$	$\frac{\left\|\varepsilon^{\mathrm{p}}_{\mathrm{coarse}} - \varepsilon^{\mathrm{p}}_{\mathrm{fine}}\right\|}{\left\|\varepsilon^{\mathrm{p}}_{\mathrm{fine}}\right\|}$ for 2000th cycle	Speed up $\frac{\text{fine scale time}}{\text{coarse scale time}}$
10^{-10}/128	25	0.003 36	29
10^{-10}/128	50	0.025 44	43
10^{-10}/128	100	0.0411	58
10^{-10}/128	∞	0.0811	67
10^{-4}/30	25	0.0105	35
10^{-4}/30	50	0.0189	53
10^{-4}/30	100	0.0373	72
10^{-4}/30	∞	0.0687	84
10^{-3}/10	25	2.324	36
10^{-3}/10	50	2.308	57
10^{-3}/10	100	2.298	74
10^{-3}/10	∞	2.308	83

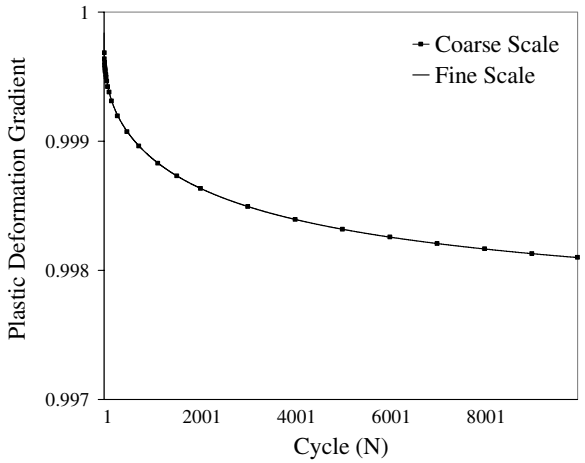

Figure 14. Coarse scale evolution of plastic deformation gradient F^{p}_0 as a function of cycles (N).

initiate a crack in a hard grain is inversely related to the non-local plastic strain gradients in the neighboring soft grain. This follows from its inverse square root relation with the dislocation pile-up length. A direct approach is proposed in this paper to evaluate the pile-up length using the distribution of GNDs inside the grain. The critical material constants in the crack nucleation criterion are calibrated using the experimental results of ultrasonic monitoring of crack evolution in dwell fatigue experiments. The calibrated criterion is successfully validated through accurate predictions of the number of cycles to failure as well as the critical features of the failure site in dwell fatigue experiments.

The significance of the criterion proposed in this paper is its sensitivity to microstructure. It should be considered as an important first step in the direction of elimination of empiricism in fatigue life prediction. There are other possibilities in terms of the evaluation of the pile-up length that are currently being investigated. The authors are currently working to change the crystal plasticity formulation to one in which the dislocation densities are used directly as

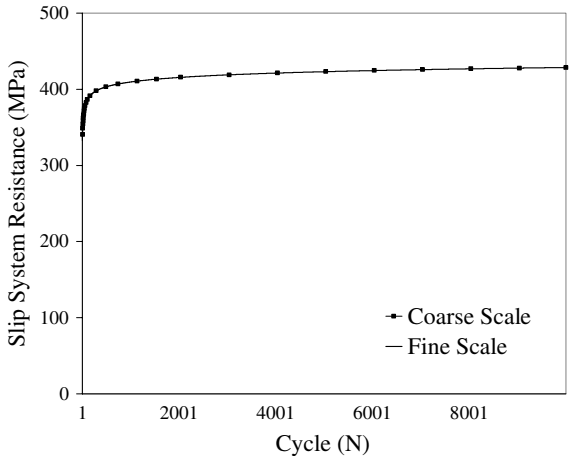

Figure 15. Coarse scale evolution of slip system resistance g_o^α as a function of cycles (N).

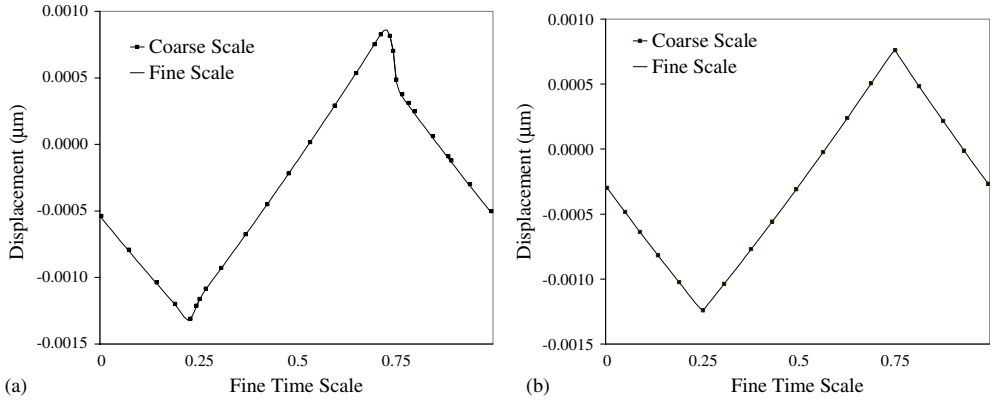

Figure 16. Displacement of a nodal degree of freedom at (a) 20th cycle and (b) 435th cycle.

variables. This would increase the computations significantly but the pile-up would be a direct outcome of these FEM calculations.

A new wavelet based multi-time scale technique that show significant potential in studying the cyclic behavior of polycrystalline alloys under all types of loading conditions is also developed. The need for the method is motivated by the large number of cycles required till fatigue crack initiation in typical polycrystalline material. Simulating such a large number of cycles remains intractable to conventional FEM based on a single time scale. Further the existing multi-time scale approaches based on asymptotic homogenization suffer severe limitations during fully or nearly full reversible loading conditions.

The multi-time scale approach presented here utilizes a wavelet decomposition of the nodal displacement variables to decouple the fine scale and coarse scale behavior during cyclic deformation. The fast varying fine scale response which necessitates the use of relatively small time steps throughout in conventional FEM simulations is effectively captured through a suitable wavelet basis. This can then be utilized to obtain the coarse scale evolution equations for the microstructural state variables. A modified FE framework required to incorporate

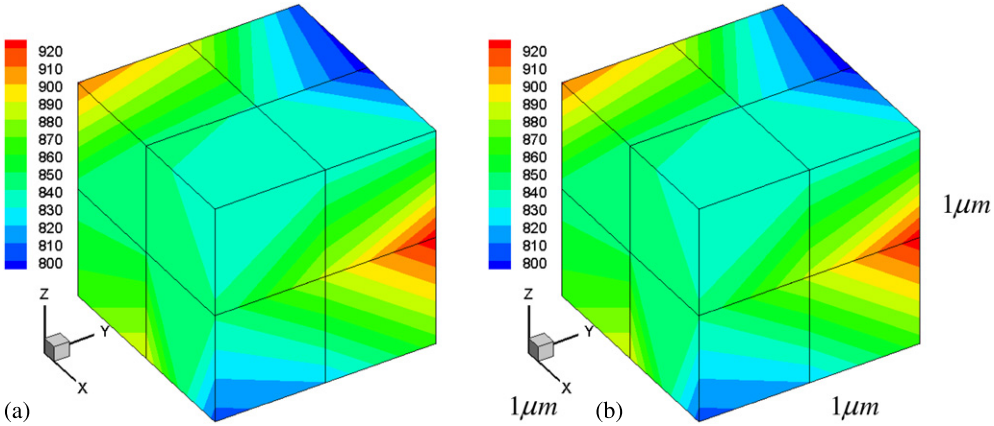

Figure 17. Stress (σ_{zz}) contour at the 10 000th cycle: (*a*) coarse scale and (*b*) fine scale.

these coarse scale equations is also developed. The coarse scale variables show an extremely smooth behavior as compared with the fine scale response and therefore can be integrated over several cycles in a single integration step resulting in significant computational savings. The microstructural fine scale response which is required for the proposed crack initiation criteria can be recovered when required given the values of the nodal displacement wavelet coefficients and the coarse scale state variables.

The cyclic response of a simplified 1D viscoplastic model and a representative 3D crystal plasticity model is studied using the developed method under fully reversible loading conditions which limits the use of existing multi-time scale schemes. The results are in excellent agreement with that of conventional FEM simulations, while obtaining a several fold improvement in the computational time.

A criterion for choosing the optimal number of wavelet coefficients is under development, along with the application of the method to study the fatigue crack initiation behavior of large polycrystalline microstructures such as the one considered in the first part of the paper.

Acknowledgments

This work has been supported by the FAA (Grant No DTFA03-01-C-0019, Program Manager: Dr Joe Wilson), Air Force Office of Scientific (Grant No FA9550-05-1-0067, Program Manager: Dr Victor Giurgiutiu) and Office of Naval Research (Grant No N00014-05-1-0504, Program Manager: Dr Julie Christodolou). Computer support by the Ohio Supercomputer Center through Grant No PAS813-2 is also acknowledged.

Appendix A. Jacobians for the 1D viscoplastic problem

In this section the Jacobians for the constitutive level and equilibrium level iterations for the 1D viscoplastic model in section 3.4.1 is derived. The state variables in the model (evolving during the cycle $N + \Delta N$) are

$$\boldsymbol{\alpha}\left(N+\Delta N,\tau\right)=\begin{Bmatrix}\varepsilon^{\mathrm{p}}\left(N+\Delta N,\tau\right)\\ g\left(N+\Delta N,\tau\right)\end{Bmatrix}. \tag{A.1}$$

The coarse time variables are

$$\boldsymbol{\alpha}_0\,(N+\Delta N)=\boldsymbol{\alpha}\,(N+\Delta N,0)=\begin{Bmatrix}\varepsilon^{\mathrm{p}}\,(N+\Delta N,0)\\ g\,(N+\Delta N,0)\end{Bmatrix}=\begin{Bmatrix}\varepsilon^{\mathrm{po}}\,(N+\Delta N)\\ g^{\mathrm{o}}\,(N+\Delta N)\end{Bmatrix}. \tag{A.2}$$

The coarse scale derivative for these variables is obtained based on equation (22) and is given by

$$\begin{aligned}\frac{\mathrm{d}\boldsymbol{\alpha}_0}{\mathrm{d}N}\,(N+\Delta N)&=\frac{\boldsymbol{\alpha}\,(N+\Delta N,T)-\boldsymbol{\alpha}\,(N+\Delta N,0)}{T}\\&=\frac{\boldsymbol{\alpha}\left(N+\Delta N,\tau_{N_{\mathrm{f}}}\right)-\boldsymbol{\alpha}\,(N+\Delta N,0)}{T}=\frac{\boldsymbol{\alpha}_{N_{\mathrm{f}}}-\boldsymbol{\alpha}_0}{T},\end{aligned} \tag{A.3}$$

where N_{f} is the number of fine scale points used to sample the displacement field at node 2. Given the value of the coarse time variable $\boldsymbol{\alpha}_0$, a backward Euler scheme (corresponding to the integral in equation (22)) is used to obtain $\boldsymbol{\alpha}_{N_{\mathrm{f}}}$ in the above equation using equation (37):

$$\boldsymbol{\alpha}_k=\boldsymbol{\alpha}_{k-1}+\dot{\boldsymbol{\alpha}}_k\Delta\tau\Rightarrow\begin{Bmatrix}\varepsilon^{\mathrm{p}}_k\\ g_k\end{Bmatrix}=\begin{Bmatrix}\varepsilon^{\mathrm{p}}_{k-1}\\ g_{k-1}\end{Bmatrix}+\begin{Bmatrix}\dot{a}\Delta\tau\left|\dfrac{\sigma_k}{g_k}\right|\operatorname{sign}(\sigma_k)\\ h\left|\varepsilon^{\mathrm{p}}_k-\varepsilon^{\mathrm{p}}_{k-1}\right|\end{Bmatrix}\qquad k=1\ldots N_{\mathrm{f}}, \tag{A.4}$$

where the subscript k indicates the variable evaluated at fine scale point τ_k and $\Delta\tau=\frac{1}{N_{\mathrm{f}}}$. Linearizing the above equation gives

$$\begin{aligned}&\mathrm{d}\boldsymbol{\alpha}_k=\boldsymbol{A}_k\mathrm{d}\boldsymbol{\alpha}_{k-1}+\begin{Bmatrix}BE/g_k\\ h\operatorname{sign}(\sigma_k)\end{Bmatrix}d\varepsilon_k\\&\text{where }\boldsymbol{A}_k=\frac{\partial\boldsymbol{\alpha}_k}{\partial\boldsymbol{\alpha}_{k-1}}=\left(\boldsymbol{I}-\begin{bmatrix}-BE/g_k & -B\sigma_k/g_k^2\\ h\operatorname{sign}(\sigma_k) & 0\end{bmatrix}\right)^{-1}\begin{bmatrix}1 & 0\\ -h\operatorname{sign}(\sigma_k) & 1\end{bmatrix}\\&B=\frac{\dot{a}\Delta\tau}{m}\left|\frac{\sigma}{g}\right|^{(1/m)-1}.\end{aligned} \tag{A.5}$$

For the constitutive level iteration, the applied strain at a point remains fixed and therefore $\mathrm{d}\varepsilon_k=0$ for all k. Applying the chain rule successively to the above equation, the following relation is obtained:

$$\left.\frac{\partial\boldsymbol{\alpha}_k}{\partial\boldsymbol{\alpha}_0}\right|_{\varepsilon}=\prod_{i=0}^{k}\boldsymbol{A}_i\qquad\text{with}\quad\boldsymbol{A}_0=\boldsymbol{I}\quad\text{and}\quad k=1\ldots N_{\mathrm{f}}. \tag{A.6}$$

Linearizing the constitutive residual equation (38) and substituting the relation in equation (A.3) results in

$$\mathrm{d}\boldsymbol{f}^{\mathrm{const}}=\gamma\mathrm{d}\boldsymbol{\alpha}_0-\frac{\Delta N}{T}\mathrm{d}\boldsymbol{\alpha}_{N_{\mathrm{f}}}\qquad\text{with }\gamma=\left(a_1+\frac{\Delta N}{T}\right). \tag{A.7}$$

Substituting equation (A.6) into the above equation gives the Jacobian for the constitutive iteration:

$$\frac{\mathrm{d}\boldsymbol{f}^{\mathrm{const}}}{\mathrm{d}\boldsymbol{\alpha}_0}=\gamma\boldsymbol{I}-\frac{\Delta N}{T}\prod_{i=0}^{N_{\mathrm{f}}}\boldsymbol{A}_i. \tag{A.8}$$

In order to calculate the Jacobian of the equilibrium iteration, the linearization is done with respect to the displacement coefficients (at node 2). Therefore, the perturbation of the applied strain at a material point- $\mathrm{d}\varepsilon_k\neq0$ and is given by

$$\mathrm{d}\varepsilon_k=\sum_{l=1}^{N_{\mathrm{evol}}}\hat{T}_{kl}\mathrm{d}\hat{q}_l, \tag{A.9}$$

where $\hat{T}_{kl}$ are components of the wavelet transform matrix in equation (31) and $\hat{q}_l$ are the evolving displacement coefficients at node 2. Using this in conjunction with equations (A.5) and (A.6), the following relation is obtained:

$$\frac{\partial \boldsymbol{\alpha}_k}{\partial \widehat{\boldsymbol{q}}} = \frac{\partial \boldsymbol{\alpha}_k}{\partial \boldsymbol{\alpha}_0}\bigg|_{\varepsilon} \frac{\partial \boldsymbol{\alpha}_0}{\partial \widehat{\boldsymbol{q}}} + \boldsymbol{A}_k \begin{Bmatrix} BE/g_k \\ h \ \mathrm{sign}\,(\sigma_k) \end{Bmatrix} \begin{bmatrix} \widehat{T}_{k1} & \dots & \widehat{T}_{kN_{\mathrm{evol}}} \end{bmatrix}. \tag{A.10}$$

Since the constitutive equation is assumed to be satisfied during equilibrium iteration, setting $d\boldsymbol{f}^{\mathrm{const}} = 0$ results in the relation

$$\mathrm{d}\boldsymbol{\alpha}_0 = \frac{\Delta N}{T\gamma} \mathrm{d}\boldsymbol{\alpha}_{N_{\mathrm{f}}}. \tag{A.11}$$

This above relationship is used along with equation (A.10) with $k = N_{\mathrm{f}}$ to obtain

$$\frac{\partial \boldsymbol{\alpha}_0}{\partial \widehat{\boldsymbol{q}}} = \left(\boldsymbol{I} - \frac{\Delta N}{T\gamma} \frac{\partial \boldsymbol{\alpha}_{N_{\mathrm{f}}}}{\partial \boldsymbol{\alpha}_0}\bigg|_{\varepsilon} \right)^{-1} \boldsymbol{A}_{N_{\mathrm{f}}} \begin{Bmatrix} BE/g_{N_{\mathrm{f}}} \\ h \ \mathrm{sign}\,(\sigma_{N_{\mathrm{f}}}) \end{Bmatrix} \begin{bmatrix} \widehat{T}_{N_{\mathrm{f}}1} & \dots & \widehat{T}_{N_{\mathrm{f}}N_{\mathrm{evol}}} \end{bmatrix}. \tag{A.12}$$

Equations (A.10) and (A.12) can be used to obtain the rate of change of the state variables $\boldsymbol{\alpha}_k$ at a given material point corresponding to fine scale point τ_k with respect to the nodal wavelet coefficients:

$$\frac{\mathrm{d}\boldsymbol{\alpha}_k}{\mathrm{d}\widehat{\boldsymbol{q}}} = \begin{Bmatrix} \dfrac{\mathrm{d}\varepsilon_k^{\mathrm{p}}}{d\widehat{\boldsymbol{q}}} \\ \dfrac{\mathrm{d}g_k}{\mathrm{d}\widehat{\boldsymbol{q}}} \end{Bmatrix}. \tag{A.13}$$

This is then used along with the linearization of the equilibrium equation (39) to obtain its Jacobian as

$$\frac{\partial f^i}{\partial q^j} = 2E\delta_{ij} + E \sum_{l=1}^{N_{\mathrm{f}}} \widehat{T}_{il} \left(\frac{\partial \varepsilon_l^{\mathrm{p}}}{\partial q_j}\bigg|_{\mathrm{elem2}} - \frac{\partial \varepsilon_l^{\mathrm{p}}}{\partial q_j}\bigg|_{\mathrm{elem1}} \right). \tag{A.14}$$

References

[1] Inman M A and Gilmore C M 1979 Room temperature creep of Ti-6Al-4V *Metall. Trans.* A **10** 419–25

[2] Hasija V, Ghosh S, Mills M J and Joseph D S 2003 Modeling deformation and creep in Ti–6Al alloys with experimental validation *Acta Mater.* **51** 4533–45

[3] Bache M R 2003 A review of dwell sensitive fatigue in titanium alloys: the role of microstructure, texture and operating conditions *Int. J. Fatigue* **25** 1079–87

[4] Deka D, Joseph D S, Ghosh S and Mills M J 2006 Crystal plasticity modeling of deformation and creep in polycrystalline Ti-6242 *Metall. Mater. Trans.* A **37** 1371–88

[5] Venkataramani G, Deka D and Ghosh S 2006 Crystal plasticity based FE model for understanding microstructural effects on creep and dwell fatigue in Ti-6242 *J. Eng. Mater. Tech. ASME* **128** 356–65

[6] Venkataramani G, Ghosh S and Mills M J 2007 A size dependent crystal plasticity finite element model for creep and load-shedding in polycrystalline titanium alloys *Acta Mater.* **55** 3971–86

[7] Ghosh S, Bhandari Y and Groeber M 2008 CAD based reconstruction of three dimensional polycrystalline microstructures from FIB generated serial sections *J. Comput. Aid. Des.* **40** 293–310

[8] Groeber M, Ghosh S, Uchic M D and Dimiduk D M 2008 A framework for automated analysis and simulation of 3D polycrystalline microstructures: part 1. Statistical characterization *Acta Mater.* **56** 1257–73

[9] Groeber M, Ghosh S, Uchic M D and Dimiduk D M 2008 A framework for automated analysis and simulation of 3D polycrystalline microstructures: part 2. Synthetic structure generation *Acta Mater.* **56** 1274–87

[10] Gao Q and Liu H W 1990 Characterization of the tip field of a discrete dislocation pileup for the development of physically based micromechanics *Metall. Trans.* A **21** 2087–89

[11] Sinha S and Ghosh S 2006 Modeling cyclic ratcheting based fatigue life of HSLA steels using crystal plasticity *Int. J. Fatigue* **28** 1690–704

[12] Bennett V P and McDowell D L 2003 Polycrystal orientation distribution effects on microslip in high cycle fatigue *Int. J. Fatigue* **25** 27–39

[13] Turkmen H S, Loge R F, Dawson P R and Miller M 2003 On the mechanical behavior of AA 7075-T6 during cyclic loading *Int. J. Fatigue* **25** 267–81
[14] Blekhman I I 2000 *Vibrational Mechanics* (Singapore: World Scientific)
[15] Thomsen J J 2004 *Vibrations and Stability: Theory, Analysis and Tools* (Berlin: Springer)
[16] Yu Q and Fish J 2002 Temporal homogenization of viscoelastic and viscoplastic solids subjected to locally periodic loading *Comput. Mech.* **29** 199–211
[17] Oskay C and Fish J 2004 Multiscale modeling fatigue for ductile materials *Int. J. Multiscale Comput. Eng.* **2** 1–25
[18] Manchiraju S, Asai M and Ghosh S 2007 A dual-time-scale finite element model for simulating cyclic deformation of polycrystalline alloys *J. Strain Anal. Eng. Des.* **42** 183–200
[19] Venkataramani G, Kirane K and Ghosh S 2008 Microstructural parameters affecting creep induced load shedding in Ti-6242 by a size dependent crystal plasticity FE model *Int. J. Plast.* **24** 428–54
[20] Acharya A and Beaudoin A J 2000 Grain-size effect in viscoplastic polycrystals at moderate strains *J. Mech. Phys. Solids* **48** 2213–30
[21] Ashby M F 1970 The deformation of plastically non-homogeneous materials *Phil Mag.* **21** 399–424
[22] Nye J F 1953 Some geometrical relations in dislocated crystals *Acta Metall.* **1** 153–62
[23] Engelen R A B, Geers M G D and Baaijens F P T 2003 Nonlocal implicit gradient-enhanced elasto-plasticity for the modeling of softening behavior *Int. J. Plast.* **19** 403–33
[24] Sinha V, Spowart J E, Mills M J and Williams J C 2006 Observations on the faceted initiation site in the dwell-fatigue tested Ti-6242 alloy: crystallographic orientation and size effects *Metall. Mater. Trans.* A **37** 1507–18
[25] Suresh S 1991 *Fatigue of Materials* (Cambridge: Cambridge University Press)
[26] Kirane K and Ghosh S 2008 A cold dwell fatigue crack nucleation criterion for polycrystalline Ti-6242 using grain-level crystal plasticity FE model *Int. J. Fatigue* **30** 2127–39
[27] Kirane K, Ghosh S, Groeber M and Bhattacharjee A 2009 Crystal plasticity finite element based grain level crack nucleation criterion for Ti-6242 alloys under dwell loading *J. Eng. Mater. Tech. ASME* **131** 23–37
[28] Stroh A N 1954 The formation of cracks as a result of plastic flow *Proc. R. Soc. Lond.* A **223** 404–14
[29] Baker I 1999 Improving the ductility of intermetallic compounds by particle-induced slip homogenization *Scr. Mater.* **41** 409–14
[30] Smith E 1979 *Dislocations and Cracks, in Dislocations in solids* ed F R N Nabarro (Amsterdam: North-Holland)
[31] Tanaka K and Mura T 1981 A dislocation model for fatigue crack initiation *J. Appl. Mech.* **48** 97–103
[32] Griffith A A 1920 The phenomena of rupture and flow in solids *Phil. Trans. R. Soc. Lond.* A **221** 163–98
[33] Ruiz G, Pandolfi A and Ortiz M 2001 Three-dimensional cohesive modeling of dynamic mixed mode fracture *Int. J. Numer. Methods Eng.* **52** 97–120
[34] Parvatareddy H and Dillard D A 1999 Effect of mode-mixity on the fracture toughness of Ti-6Al-4V/FM-5 adhesive joints *Int. J. Fracture* **96** 215–28
[35] Rokhlin S, Kim J Y and Zoofan B 2005 The Ohio State University, Columbus, OH, unpublished research
[36] Williams *et al* 2006 The evaluation of cold dwell fatigue in Ti-6242 *FAA Report Summary* The Ohio State University
[37] Walker J S 1999 *A Primer on Wavelets and Their Scientific Applications* (Boca Raton, FL: CRC Press)
[38] Strang G and Nguyen T 1996 *Wavelets and Filter Banks* (Wellesley, MA: Wellesley Cambridge Press)
[39] Crisfield M A 1996 *Non-Linear Finite Element Analysis of Solids and Continua* (New York: Academic)
[40] Bathe K J 1995 *Finite Element Procedures* (Englewood Cliffs, NJ: Prentice-Hall)